Fakultät für Physik und Astronomie
Ruprecht-Karls-Universität Heidelberg

Masterarbeit

im Studiengang Physik

vorgelegt von

Julian Mayr

aus Unna

2024

Complex Langevin Methoden

für die Analyse des Spin-1 Bose Gases

Masterarbeit

Die Masterarbeit wurde von Julian Mayr

ausgeführt am

Kirchhoff-Institut für Physik

unter der Betreuung von

Herrn Prof. Thomas Gasenzer

und

Herrn Prof. Jan M. Pawlowski

Department of Physics and Astronomy
University of Heidelberg

Master thesis

in Physics

submitted by

Julian Mayr

born in Unna

2024

Complex Langevin Methods

for Analysis of the Spin-1 Bose Gas

Master thesis

This Master thesis has been carried out by Julian Mayr

at the

Kirchhoff-Institute for Physics

under the supervision of

Prof. Thomas Gasenzer

and

Prof. Jan M. Pawlowski

Erklärung:

Ich versichere, dass ich diese Arbeit selbstständig verfasst habe und keine anderen als die angegebenen Quellen und Hilfsmittel benutzt habe.

Heidelberg, den 05.02.2024 Julian Mayr

Acknowledgement

I thank Philipp Heinen and Thomas Gasenzer for supervising this thesis. I also thank Kevin Ackermann and Corinna Steffen for their help with writing it. Finally, I thank all my group members for helpful and interesting conversations.
I acknowledge support by the state of Baden-Württemberg through bwHPC.

Zusammenfassung

Bose Einstein Kondensate sind physikalisch interessant aufgrund ihrer makroskopischen Quanteneigenschaften. Ihr Gleichgewichtsverhalten wird durch Näherungen wie der Bogoliubov-Theorie gut beschrieben, für Präzisionsmessungen müssen jedoch Quantenkorrekturen höherer Ordnung berücksichtigt werden. Die Zustandssumme von interagierenden Bose Gasen ist jedoch aufgrund des Vorzeichenproblems in ihrer Pfadintegralrepräsentation für normale Monte Carlo Methoden nicht zugänglich. In dieser Arbeit führen wir Monte Carlo Simulationen für das Spin-1 Bose Gas mit der complex Langevin Methode durch, um das Vorzeichenproblem zu beheben. Wir adaptieren Techniken aus anderen Monte Carlo Methoden zu complex Langevin und erhöhen dadurch dessen Effizienz. Mithilfe dieser Techniken berechnen wir aus unserer exakten Simulation Korrekturen zu bekannten Näherungsgrößen. Zuletzt zeigen wir, dass die Berechnung von Quantenverschränkung durch den Replika-Trick mit der complex Langevin Methode möglich ist, und messen Verschränkungsmaße im Spin-1 Gas.

Abstract

Bose Einstein condensates are of high physical interest due to their macroscopic quantum properties. Their equilibrium behavior is well described by approximations like Bogoliubov theory. However, when making precision measurements at criticality, higher order quantum corrections have to be taken into account. The partition sum of interacting Bose gases is however inaccesible to standard Monte Carlo methods, due to a sign problem in its path integral representation. In this thesis, we perform Monte Carlo simulations of the spin-1 Bose gas in equilibrium, using the complex Langevin method to deal with the sign problem. We adapt techniques from other Monte Carlo schemes to complex Langevin to increase its efficiency. We then use these techniques to measure the corrections to known approximations that result from out exact method. Finally, we show that quantum entanglement calculation using the replica trick is possible in complex Langevin simulations, and extract entanglement measures at and away from criticality.

Contents

Chapter 1

Summary

In this thesis, we first introduce the formalisms of many body quantum field theory, Monte Carlo with the Langevin equation, the spin-1 Bose gas, and (quantum) phase transitions. For many body QFT, we introduce the coherent state path integral, which transforms the matrix trace quantum partition function into a more useful functional integral. We then quickly cover the idea behind importance sampling and introduce the Metropolis algorithm, and demonstrate the sign problem arising due to complex actions. Solutions to the sign problem are presented, and a more in depth introduction is given for complex Langevin, which is the focus of this thesis. We then cover the low energy scattering theory of the spin-1 gas, and cover its mean field and Bogoliubov theory. Finally, we give a quick introduction to scaling and quantum phase transitions, whose properties will be useful later.

We then introduce new numerical methods we adapted to complex Langevin. We start with kernel acceleration, which helps overcome critical slowing down that plagues Monte Carlo at phase transition. Next, we adapt histogram reweighting to complex actions. This helps with reducing compute time when performing simulations of continuous parameter regimes. Finally we show how to handly measure quantum entanglement in lattice field theory, and mention the additional problems arising in complex actions.

We then perform complex Langevin analysis on some properties of the spin-1 gas. First, Bogoliubov theory is confirmed by measuring finite momentum occupation numbers. Next, we determine the critical line of the thermal phase transition from the Easy Plane into the polar phase. We find a significant deviation from the best available approximation. We also determine the shift of the quantum critical point. Finally, we perform entanglement measurement using the third Renyi negativity, and confirm the entanglement's area law scaling. We then determine the differential negativity at and away from the phase transition and find no significant shift.

Chapter 2

Introduction

For simplicity, we set the Plank constant $\hbar = 1$, and the Boltzmann constant $k_B = 1$ throughout the whole thesis.

2.1 Field Theoretical Description of Many Body Systems

2.1.1 Many Body Quantum Theory

In standard quantum mechanics, a quantum system is described by the Schroedinger equation

$$\hat{H} |\psi\rangle = E |\psi\rangle \tag{2.1}$$

with $|\psi\rangle = \psi(x_1, \ldots, x_n)$ being an n-particle wavefunction in quantum mechanical Hilbert space. While the Schroedinger equation successfully describes systems with constant particle number, it cannot describe a system where particles are created and annihilated. These processes are common in high energy physics, where particles collide and create others in particle colliders. It can also happen in low energy scattering, for example through spin changing collisions, or in statistical physics, where particles can enter and leave the system in the grand canonical ensemble. To incorporate these processes, one has to upgrade the Hilbert space to Fock space. The Fock space is a combination of all N-particle Hilbert spaces [1]

$$\mathcal{F} = S_{\pm} (\mathbb{C} \oplus \mathcal{H} \oplus \mathcal{H} \otimes \mathcal{H} \oplus \ldots) \tag{2.2}$$

with $S_{\pm}$ being the (anti)symmetrization operator, enforcing indistinguishably between particles and (anti)commutation relations between bosons (fermions). In the following, we focus on the case of bosons, which are this thesis' main concern.
The standard way of practical Fock space construction is by introducing the many particle vacuum state $|0\rangle$, the unique state of the $N = 0$ Hilbert space. We also introduce conjugate creation and annihilation operators $a_k^\dagger$, a_k for particles with momentum k [1]. We introduce

[1] We assume here a system in a box, making momentum space discrete. For the limit $V \to \infty$, the operator spectrum would become continuous, $a_k \to a(k)$, $\delta_{kq} \to \delta(k - q)$. It is usually more advantageous

canonical commutation relations [2]

$$[a_k, a_q] = \left[a_k^\dagger, a_q^\dagger\right] = 0 \tag{2.3}$$

$$\left[a_k, a_q^\dagger\right] = \delta_{kq} \tag{2.4}$$

and define the vacuum state as

$$a_k \left|0\right\rangle = 0 \tag{2.5}$$

$$\langle 0|0\rangle = 1 \tag{2.6}$$

By identifying $n_k = a_k^\dagger a_k$ as the particle number operator, it becomes clear that

$$n_k (a_k^\dagger)^N \left|0\right\rangle = N (a_k^\dagger)^N \left|0\right\rangle \tag{2.7}$$

We thus find a orthogonal basis of particle number states by defining

$$\left|N_{k_1}, N_{k_2}, \ldots\right\rangle = (a_{k_1}^\dagger)^{N_{k_1}} (a_{k_2}^\dagger)^{N_{k_2}} \ldots \left|0\right\rangle . \tag{2.8}$$

To recover Schroedinger quantum mechanics, we need to express operators acting on the wave function as operators acting on Fock space. Therefore first define the field operator

$$\hat{\phi}(x) = \sum_k e^{-ikx} \phi(x) a_k^\dagger \tag{2.9}$$

with ϕ being the standard Schroedinger wave function. Any N particle operator $\hat{O}$ acting on the wave function may be expressed in terms of ladder operators in the form [3]

$$\hat{O}(k, q, ...) = \sum_{ijkl...} a_i^\dagger a_j^\dagger \ldots o_{ij...kl...} a_k a_l \ldots \tag{2.10}$$

If $o_{ijkl} \neq 0$ for $ij \neq kl$, the operator is called non-diagonal (in momentum space). This can equivalently be done in real space using field operators. For a two body potential

$$\hat{V}(x - y) = \int_x \int_y \hat{\phi}^\dagger(x) \hat{\phi}^\dagger(y) V(x - y) \hat{\phi}(x) \hat{\phi}(y) \tag{2.11}$$

the potential is diagonal in real space, but not momentum space.

2.1.2 Coherent State Path Integral

The partition function of a quantum system in thermal equilibrium is given by [3]

$$Z = \mathrm{Tr}\left(e^{-\beta \hat{H}}\right) \tag{2.12}$$

to take this limit at the end of the calculation.

with Hamiltonian $\hat{H}$ and inverse temperature $\beta = \frac{1}{T}$. Calculating the quantum partition function is in general highly nontrivial, especially due to the exponential scaling of Hilbert space dimension with particle number. The partition function can alternatively be represented through the coherent state path integral. We derive it here following the notes of Jarrel [4]

Coherent States

In single particle quantum mechanics the coherent states $|\alpha\rangle$ are defined as eigenstates of the annihilation operator [4]

$$\hat{a}\,|\alpha\rangle = \alpha\,|\alpha\rangle \tag{2.13}$$

with $\alpha \in \mathbb{C}$. Similarly, in many body theory, coherent states are defined as

$$a_k\,|\phi\rangle = \phi_k\,|\phi\rangle \tag{2.14}$$

where $\phi_k \in \mathbb{C}$ is now a different complex number for each momentum. One can show that this definition results in

$$|\phi\rangle = e^{\sum_k \phi_k a_k^\dagger}. \tag{2.15}$$

The coherent states are not orthogonal

$$\langle\theta|\phi\rangle = e^{\sum_k \bar{\theta}_k \phi_k} \tag{2.16}$$

and (in our definition) not normalized

$$\langle\phi|\phi\rangle = e^{\sum_k \bar{\phi}_k \phi_k} \tag{2.17}$$

However, they do provide an identity operator

$$\int \prod_i \frac{d\bar{\phi}_i d\phi_i}{\pi} e^{-\sum_k \bar{\phi}_k \phi_k} |\phi\rangle\langle\phi| = \mathbb{1}_{\mathcal{F}}. \tag{2.18}$$

This can be proven by Schur's lemma, showing a_k and $a_k^\dagger$ both commute with the expression.

Coherent State Path Integral

The coherent states provide a way of rewriting the partition function. Going forward, we drop the index k from coherent state numbers and write the scalar product as $\bar{\theta}\phi = \sum_k \bar{\theta}_k \phi_k = \int d^3x \bar{\theta}(x)\phi(x)$. We also symbolically write the identity (eq. (2.18)) as $\mathbb{1} = \sum_\phi e^{-\bar{\phi}\phi}\,|\phi\rangle\,\langle\phi|$. In the same way, we rewrite the trace in (eq. (2.12)) as

$$Z = \sum_{\phi_0} \langle\phi_0|e^{-\beta\hat{H}}|\phi_0\rangle\,. \tag{2.19}$$

We then split the exponential into $M \in \mathbb{N}$ pieces, and write

$$Z = \prod_{i=0}^{M} \sum_{\phi_i, \phi_{i+1}} e^{-\bar{\phi}_i \phi_i} \left\langle \phi_{i+1} \right| e^{-\frac{\beta}{M} \hat{H}} \left| \phi_i \right\rangle . \tag{2.20}$$

Due to the trace, we identify $\phi_M = \phi_0$. The split into small time steps is valid, since its error scales quadratically in the step $1/M$ according to the BCH-Formula [5]

$$e^{\hat{X}} e^{\hat{Y}} = e^{\hat{X} + \hat{Y} + \frac{1}{2}[\hat{X}, \hat{Y}] + \cdots}. \tag{2.21}$$

If M is large enough, the exponentials in the product eq. (2.20) are quasi-linear, which means the operators $a_k^\dagger$ and a_k in $\hat{H}$ can be replaced with $\bar{\phi}_{i+1}$ and ϕ_i[2]. This converts H from an operator into a function of complex numbers. We can then write

$$Z = \prod_{i=0}^{M} \sum_{\phi_i, \phi_{i+1}} e^{-\bar{\phi}_i \phi_i} \left\langle \phi_{i+1} | \phi_i \right\rangle e^{-\frac{\beta}{M} H(\bar{\phi}_{i+1}, \phi_i)} \tag{2.22}$$

$$= \prod_{i=0}^{M} \sum_{\phi_i, \phi_{i+1}} e^{-\bar{\phi}_i \phi_i + \bar{\phi}_{i+1} \phi_i - \frac{\beta}{M} H(\bar{\phi}_{i+1}, \phi_i)} \tag{2.23}$$

$$= \prod_{i=0}^{M} \sum_{\phi_i, \phi_{i+1}} e^{\phi_i (\bar{\phi}_{i+1} - \bar{\phi}_i) - \frac{\beta}{M} H(\bar{\phi}_{i+1}, \phi_i)} \tag{2.24}$$

and reintroduce integral notation for the scalar product

$$Z = \int \prod_{i=0}^{M} \prod_{x} \left(d\bar{\phi}_i(x) d\phi_i(x) \right) \prod_{i=0}^{M} \left(e^{\int d^3x (\phi_i (\bar{\phi}_{i+1} - \bar{\phi}_i) - \frac{\beta}{M} H(\bar{\phi}_{i+1}, \phi_i))} \right) \tag{2.25}$$

dropping π factors appearing in the identity eq. (2.18). The product over x runs over infinitely many positions, or a finite number if discretized on a lattice. eq. (2.25) is the coherent state path integral in its discrete form, which is used for numerics in this thesis. One may take the continuum limit by introducing $\Delta = \frac{\beta}{M}$, identifying the index i with an imaginary time dimension τ, and introducing path integral notation $D\phi = \prod_x \prod_{i=0}^{M} \left(d\bar{\phi}_i d\phi_i \right)$

$$Z = \int D\phi \prod_{i=0}^{M} e^{\int d^3x (\Delta (\phi_i \frac{(\bar{\phi}_{i+1} - \bar{\phi}_i)}{\Delta} - H(\bar{\phi}_{i+1}, \phi_i)))} \tag{2.26}$$

$$= \int D\phi e^{\int d^3x \oint_0^\beta d\tau (\phi \partial_\tau \bar{\phi} - H(\bar{\phi}, \phi))}. \tag{2.27}$$

[2] This only applies for a Hamiltonian in normal order, i.e. all creation operators are left of all annihilation operators, which is a trivial transformation for most Hamiltonians. An alternative way of constructing the CSPI is possible, using the diagonal representation of the Hamiltonian in the coherent states. This is not as easy to find, especially for many body coherent states. It might have some advantages due to its better discretization [6].

This is a functional integral known from high energy physics, and $\oint_0^\beta d\tau(-\phi\partial_\tau\bar{\phi} + H(\bar{\phi},\phi))$ can be identified as a non-relativistic action $S[\phi]$. Although the continuum limit is well defined, one still has to respect the discretization specified in eq. (2.25) to get correct results when implementing it in a discretized way.
The path integral expression for observables is found in the same manner

$$\begin{aligned}\langle a^\dagger a\rangle &= \mathrm{Tr}(e^{-\beta H}a^\dagger a)/Z \qquad (2.28)\\ &= \dots \\ &= \frac{1}{Z}\int\left\{\prod_{i=0}^{M}\prod_x \left(d\bar{\phi}_i(x)d\phi_i(x)\right)\prod_{i=0}^{M}\left(e^{\int d^3x(\phi_i(\bar{\phi}_{i+1}-\bar{\phi}_i)-\frac{\beta}{M}H(\bar{\phi}_{i+1},\phi_i))}\right)\bar{\phi}_M\phi_{M-1}\right\} \qquad (2.29)\end{aligned}$$

evaluating $\bar{\phi}$ and ϕ at different time steps. Due to imaginary time translation symmetry, one may also write

$$\langle a^\dagger a\rangle = \frac{1}{Z}\int\left\{\prod_{i=0}^{M}\prod_x \left(d\bar{\phi}_i(x)d\phi_i(x)\right)\prod_{i=0}^{M}\left(e^{\int d^3x(\phi_i(\bar{\phi}_{i+1}-\bar{\phi}_i)-\frac{\beta}{M}H(\bar{\phi}_{i+1},\phi_i))}\right)\left(\frac{1}{M}\sum_{n=0}^{M}\bar{\phi}_n\phi_{n-1}\right)\right\} \qquad (2.30)$$

which is more convenient for Monte Carlo simulations.

Comparison to Real Time

The discussed construction of the coherent state path integral for the equilibrium partition function is also possible for real time evolution of a state. The amplitude describing the evolution from state $|i\rangle$ to $|f\rangle$ is then

$$M_{fi} = \langle . \rangle \qquad (2.31)$$

Expanding $|f\rangle$ and $|i\rangle$ in the basis of the coherent states [4]

$$\langle f| = \int\prod_j \frac{d\bar{\phi}_j(t_f)d\phi_j(t_f)}{\pi}e^{-\sum_k\bar{\phi}_k\phi_k}\bar{\psi}_f(\phi(t_f))|\phi\rangle \qquad (2.32)$$

$$|i\rangle = \int\prod_j \frac{d\bar{\phi}_j(t_i)d\phi_j(t_i)}{\pi}e^{-\sum_k\bar{\phi}_k\phi_k}\psi_i(\bar{\phi}(t_i))|\phi\rangle \qquad (2.33)$$

we find the result

$$\langle\psi_f|e^{-i\hat{H}t}|\psi_i\rangle = \int D\phi e^{i\int_0^t dt(i\phi\partial_t\bar{\phi}-H(\bar{\phi},\phi))}\times\bar{\psi}_f(\phi(t_f))\psi_i(\bar{\phi}(t_i))e^{\frac{1}{2}(\bar{\phi}(t_f)\phi(t_f)+\bar{\phi}(t_i)\phi(t_i))}. \qquad (2.34)$$

The construction of the CSPI is done analogously, with β replaced by it. For this reason, the thermal path integral is often called the *imaginary time path integral*. Only a Wick

rotation $t \to -i\beta$ [7] is needed to get the real time version. In a similar manner, using the Schwinger-Keldysh [7] formalism, it is possible to construct path integrals on general closed curves in the complex plane. This allows, for example, calculating real time correlators in thermal equilibrium. However, the real and complex versions of the path integral exhibit a much stronger *sign problem* than the imaginary one (see [8][9][10] on ongoing research for real time simulations). Therefore, this thesis focuses on the imaginary time version.

2.2 Complex Langevin Simulation

2.2.1 Monte Carlo and Importance Sampling

In classical mechanics, a statistical system in equilibrium is described by its partition function

$$Z = \sum_x e^{-\beta H(x)} \tag{2.35}$$

where the sum goes over all possible states of the system, and H is a classical Hamiltonian. The partition function is the normalization of the probability density function

$$P(x) = \frac{e^{-\beta H(x)}}{\sum_y e^{-\beta H(y)}} = \frac{e^{-\beta H}}{Z}. \tag{2.36}$$

Often the expectation values of macroscopic observables are more important than the probability of single configuration. They are defined as

$$\langle O \rangle = \sum_x P(x) O(x) \tag{2.37}$$

with x again running over all possible states. For finite discrete systems, performing this sum numerically is possible, as long as the system is small. However, the amount of possible states of most systems scales exponentially with their size; for example, the Ising model has a total state space size of $2^{\#\text{lattice sites}}$.[3] In some cases, it might be possible to evaluate this sum analytically. Examples include the 1D and 2D Ising model, or the ideal gas. In this work we are interested in approximating the sum numerically. One possible way of doing that is to uniformly sample M random states y_i from the possible states in the state space and calculate [11]

$$\langle O \rangle \approx \frac{\sum_{i=0}^{M} P(y_i) O(y_i)}{\sum_{i=0}^{M} P(y_i)}. \tag{2.38}$$

For large enough M, this will approximate the observable. Performing averages over uniformly sampled states to compute an observable like eq. (2.38) is the simplest form of a Monte Carlo algorithm. However, this approximation converges towards the true value $\langle O \rangle$ very slowly. The slow convergence is quite easy to understand: For most systems in equilib-

[3] It also has a number of symmetries reducing the relevant state space, which allows for analytic solutions.

rium, most states are highly unlikely. An Ising magnet for example only experiences small thermal fluctuations around its average magnetization. It is very unlikely to drift far away from it, which means most states have a probability of almost zero. Thus, the states that actually occur in the physical system with a reasonable probability are very unlikely to be sampled.

The aim of *importance sampling* [11] is to not sample from the system uniformly, but instead according to the probability distribution $P(x)$. We may rewrite the sum in (eq. (2.37))

$$\langle O \rangle = \sum_x O(x) \frac{P(x)}{Q(x)} Q(x) \tag{2.39}$$

with another probability density Q. When sampling from the density Q instead of a uniform density, eq. (2.38) becomes

$$\langle O \rangle \approx \frac{\sum_{i=0}^{M} \frac{P(y_i)}{Q(y_i)} O(y_i)}{\sum_{i=0}^{M} \frac{P(y_i)}{Q(y_i)}}. \tag{2.40}$$

The obvious choice of Q to optimize sampling seems to be $Q = P$. Observables are then calculated as

$$\langle O \rangle \approx \frac{1}{M} \sum_y O(y) \tag{2.41}$$

eliminating the probability from the average, since it is already accounted for by the sampling process. The states sampled are now also those that practically occur in the system, making the averaging much more efficient. However, sampling from an arbitrary probability distribution is nontrivial. There most important algorithms to perform this sampling are so called *Markov chain Monte Carlo* algorithms [12], which work by transitioning from a sampled state Y_t to Y_{t+1} with probability $P(Y_t \to Y_{t+1})$. They transition from state to state repeatedly, generating a Markov chain of states Y_t. The observable in the $t \to \infty$ limit is

$$\langle O \rangle = \lim_{M \to \infty} \frac{1}{M} \sum_{t=0}^{M} O(Y_t). \tag{2.42}$$

In practice, the process is to first run the algorithm to a fixed number of steps to reach the equilibrium distribution, and then to sample states until sufficient statistical accuracy is reached. To sample from a probability density, the process then has to fulfill two properties: Ergodicity and detailed balance. Following [12], we show how these properties lead us to the Metropolis algorithm.

Ergodicity means that the sampling process must be able to reach any state in the system from any other state; there may not be any impassible barriers. This makes sense from a physical perspective: A gas cannot pass through walls to equilibrate. Walls that the gas has to go around are still possible.

Detailed balance is what guarantees that we sample from the given probability distribution

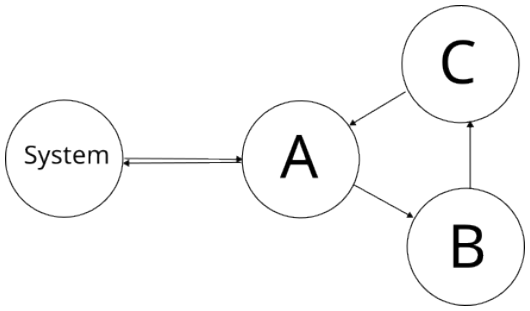

(a) Three states with a limit cycle. There is a nonzero probability flow in direction $A \to B \to C$

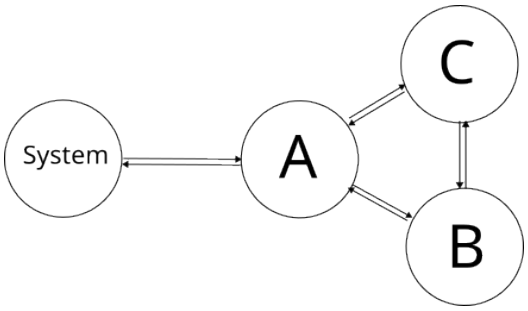

(b) The same three states with detailed balance enforced. The net probability flow is zero

Figure 2.1: A system with and without detailed balance. Both systems can share the same equilibrium distribution, but the left one may not converge towards it.

Q, rather than any other one. To have Q as an equilibrium distribution, the Markov process must fulfill [12]

$$\sum_Y Q(X)P(X \to Y) = \sum_Y Q(Y)P(Y \to X). \tag{2.43}$$

If we assume $P(X \to Y)$ to be normalized over target states Y, this becomes

$$Q(X) = \sum_Y Q(Y)P(Y \to X). \tag{2.44}$$

However, the system does not have to converge to the equilibrium distribution, as it may get stuck in a *limit cycle*, a set of states that it may fall into and cycle around, see fig. 2.1. This leads to a dynamic equilibrium, where the PDF doesn't converge but periodically changes. To prevent limit cycles, we need to enforce the detailed balance condition

$$Q(X)P(X \to Y) = Q(Y)P(Y \to X) \tag{2.45}$$

from which also directly follows eq. (2.43) by summing over both sides. This condition breaks the possibility of cycles, since the overall number of transitions $X \to Y$ happening must be equal to those $Y \to X$ happening. In a cycle, one direction must be preferred.
The detailed balance conditions leads us to the simplest implementation of a Monte Carlo algorithm, the Metropolis algorithm. Rearranging eq. (2.45) gives us

$$\frac{P(X \to Y)}{P(Y \to X)} = \frac{Q(Y)}{Q(X)}. \tag{2.46}$$

We can now implement a selection-acceptance scheme, where we randomly sample a transition with a probability distribution $g(X \to Y)$ that is known well, and then accept this transition with acceptance probability $A(X \to Y)$. Then $P(X \to Y) = g(X \to Y)A(X \to Y)$. Consider a simple Ising model with N sites. We, at each step, choose one site k where the

spin is flipped, and leave the rest as is. The transition probabilities are then

$$g(X \to Y) = \frac{1}{N}. \tag{2.47}$$

This means that

$$\frac{P(X \to Y)}{P(Y \to X)} = \frac{A(X \to Y)}{A(Y \to X)} = \frac{Q(Y)}{Q(X)}. \tag{2.48}$$

It can be seen that the choice

$$A(X \to Y) = \begin{cases} \frac{Q(Y)}{Q(X)} & \text{if } \frac{Q(Y)}{Q(X)} < 1 \\ 1 & \text{otherwise.} \end{cases} \tag{2.49}$$

fulfills this condition. This choice is not unique, but it is the choice that maximizes acceptance rates [12], which is crucial for algorithm runtime. Since being invented by Metropolis et al in 1953 [13], any algorithm with acceptance probabilities in the form of eq. (2.49) is called a Metropolis algorithm. In this thesis, we actually use a non-Metropolis sampling scheme by using the Langevin equation. In systems without a sign problem, even the Langevin method is usually coupled with a Metropolis style accept/reject step, with Langevin steps instead of random sampling yielding higher acceptance rates. This is called hybrid or Hamiltonian Monte Carlo (HMC)[14].

2.2.2 The Sign Problem

Sampling from quantum systems is generally not as simple. The partition function (eq. (2.12)), is now given by a matrix trace [3] and observables are calculated through $\mathrm{Tr}(\hat{O}e^{-\beta\hat{H}})$. Sampling from this partition function is still possible, using so called *Quantum Monte Carlo* algorithms. These usually work directly with the many-particle wavefunction, making them constrained in the number of particles [15]. An alternative is using a field theoretic path integral representation of the partition function, as introduced in the section 2.1.2. For many systems in equilibrium, using the path integral allows Monte Carlo sampling in the same way as for classical systems. Examples include lattice quantum chromodynamics (QCD) [16] without chemical potential, scalar ϕ^4 theory [17], and some quantum spin models [18]. There are however systems for which the partition function is not positive definite, i.e. the probability of a state can become complex [19]. This is called the sign problem [19]. One such example has already been introduced with the CSPI (eq. (2.27)), where the first order derivative $\phi\partial_\tau\bar{\phi}$ is imaginary, easiest seen by rewriting it as $i\omega\phi\bar{\phi}$ in Fourier space. While such complex probability density functions are not PDFs in the strict sense, it can be shown that, for all physical observables, it holds that [19]

$$\langle O \rangle = \sum_x P(x)O(x) \in \mathbb{R}. \tag{2.50}$$

Thus, while the probabilities of single states might be complex, for every real observable, the expectation value averages to be real. This averaging can be compared to Wigner functions in Wigner quantization [20], where the Wigner function $W(X,P)$ might be complex, but the marginals $W(X) = \int_P W(X,P)$, $W(P) = \int_X W(X,P)$ are positive definite and proper PDFs. One may interpret that while these complex probabilities exist, they are protected from being observed by Heisenberg's uncertainty principle.

2.2.3 Approaches to the Sign Problem

Since the Metropolis algorithm relies on comparison of probabilities, it cannot be applied to systems with complex probabilities, for which there is no ordering. Other approaches to sampling from complex PDFs exist (for a review see [21],[19]), some of which are briefly discussed before focusing on this thesis' method of choice, complex Langevin. We follow here [21].

Reweighting

The obvious and simplest solution to enable Monte Carlo sampling on complex PDFs is reweighting. Often, the sign problem results from a single imaginary term in the Lagrangian, like the first order time derivative in the CSPI. This term is then absorbed into the observable, and the sampling is done on the remainder of the PDF. For example, for the CSPI

$$\langle O \rangle = \frac{1}{Z} \sum_{\phi} O(\phi) e^{\oint_0^\beta d\tau (\phi \partial_\tau \bar{\phi} - H(\bar{\phi},\phi))} \tag{2.51}$$

$$= \frac{1}{Z} \sum_{\phi} \left(O(\phi) e^{\oint_0^\beta d\tau \phi \partial_\tau \bar{\phi}} \right) e^{-\oint_0^\beta d\tau H(\bar{\phi},\phi)} \tag{2.52}$$

$$= \frac{1}{Z} \sum_{\phi} O'(\phi) e^{-\oint_0^\beta d\tau H(\bar{\phi},\phi)}. \tag{2.53}$$

The remainder PDF $e^{-\oint_0^\beta d\tau H(\bar{\phi},\phi)}$ is now purely real and standard Monte Carlo algorithms can be used. The observable O' gains an imaginary part in single realizations that averages out in the expectation value. While reweighting technically enables the use of Monte Carlo algorithms, it also makes them more inefficient. Since only a remainder of the PDF is used for sampling, the time complexity of the algorithm is increased. It can easily be seen that for the "most severe" sign problem, a purely imaginary term in the exponential, the whole PDF would have to be absorbed into the observable, which would mean

$$\langle O \rangle = \frac{1}{Z} \sum_{\phi} (O(\phi) e^{-iS[\phi]}) \times 1 \tag{2.54}$$

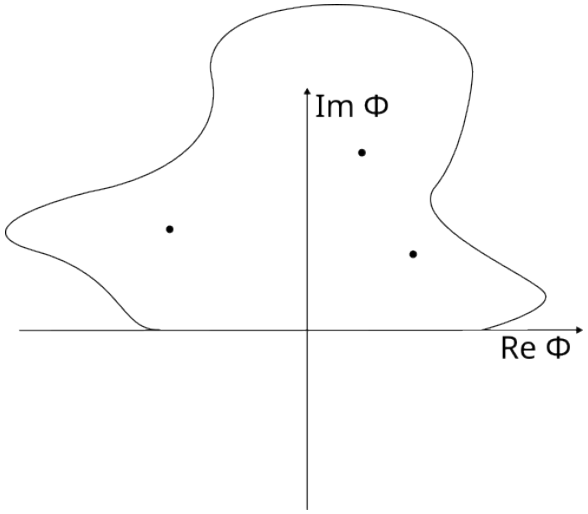

Figure 2.2: A contour deformation of a real integral from $-\infty$ to ∞. As long as the deformation doesn't cross the poles (marked as dots), the value of the integral won't change.

with a remainder PDF $P(\phi) = \frac{1}{Z}$. This reduces importance sampling to uniform sampling. Therefore, reweighting can only be used when the sign problem is minor, i.e. the complex term is very small in comparison to the rest of the Langrangian.

Alternative Variables

In some cases, the sign problem might merely be an algebraic problem, solved by rewriting the partition function in terms of new variables. This may be by introducing auxiliary fields in a Hubbard-Stratonovich transformation, or by rewriting the imaginary part of the partition function as a constraint on new, discrete variables. This can solve the sign problem in a lot of bosonic systems.

Lefshetz Thimbles

Another idea is to change the integration contour instead of the variables themselves. For example, for a one-site model, we may deform the integration boundaries

$$Z = \int_{-\infty}^{\infty} e^{-S[\phi]} d\phi \tag{2.55}$$

$$= \int_{\mathcal{C}} e^{-S[\phi]} d\phi \tag{2.56}$$

where the new contour $\mathcal{C}$ is now a continuous deformation of the real line into complex space, and ϕ is complexified (fig. 2.2). If the integrand is analytic, this doesn't change the physics. A *Lefshetz Thimble* is a contour on which the imaginary part of $S[\phi]$ is (approximately) constant. If such a contour can be found, it is then possible to determine the partition function with standard Monte Carlo methods on the thimble, maybe using reweighting if

the thimble is approximate. These thimbles are usually found by a gradient descent method

$$\frac{d\phi}{dt} = -\left(\frac{\delta S}{\delta \phi}\right)^* \tag{2.57}$$

towards stationary points in the imaginary part of $S[\phi]$. Some problems remain, like the residual sign problem on a numerically found thimble, and the global sign problem due to contributions from multiple thimbles. Nevertheless, Lefshetz Thimbles have been applied to a variety of problems e.g. in lattice QCD and Hubbard models.

2.2.4 Complex Langevin

Complex Langevin is another approach to the sign problem employing complexified variables. However, instead of trying to minimize the sign problem like Lefshetz Thimbles, it uses the complex variables to perform stochastic Langevin evolution of the fields.

Classical Langevin

The Langevin equation originally stems from stochastic dynamics like Brownian motion, modeling the motion of a small particle under random molecular collisions [22]. The probability distribution of the particle's position may be derived from the stochastic differential equation describing its motion. We make use of the inverse mapping, starting out with a probability density and deriving a stochastic differential equation describing it. For a real field ϕ, the Langevin equation reads [21]

$$\frac{d\phi}{d\theta} = -\frac{\delta S}{\delta \phi} + \eta \tag{2.58}$$

where we introduced a new Langevin time θ in which the field evolves stochastically. The first term on the RHS of eq. (2.58) is called the *drift term*. It drives the system towards its classical solution, where the action is minimized. The second term is the *noise term*. It consists of stochastic Wigner noise, i.e. white noise with correlation $\eta(\theta)\eta(\theta') \propto \delta(\theta - \theta')$. The stochastic noise can more easily be quantified in the discretized equation

$$\phi_{\theta+\Delta\theta}(x) = \phi_\theta - \Delta\theta \frac{\delta S}{\delta \phi_\theta(x)} + \sqrt{2\Delta\theta}\eta(x) \tag{2.59}$$

where $\eta(x)$ is now usually chosen as Gaussian noise with $\langle \eta(x)\eta(y)\rangle = \delta(x-y)$. Uniform noise is possible but rarely used [23].
We want to show that the stochastic process eq. (2.58) samples from the PDF $P[\phi] \propto e^{-S[\phi]}$. We therefore need to look at the process' Fokker-Planck equation. The Fokker-Planck equation is an equation describing the evolution of the probability density $P(\phi, \theta)$ corresponding to a stochastic process on ϕ. In the following derivation we assume, for simplicity, a one component, 0+1d real scalar field ϕ. It is easily possible to generalize to

any number of variables. The Fokker-Planck equation corresponding to eq. (2.58) is given by [24]

$$\frac{\partial P(\phi,\theta)}{\partial \theta} = \frac{\partial}{\partial \phi}\left[\frac{\partial S[\phi]}{\partial \phi} P(\phi,\theta)\right] + \frac{\partial^2 P(\phi,\theta)}{\partial \phi^2}. \tag{2.60}$$

A steady state, equilibrium distribution thus requires

$$\frac{\partial}{\partial \phi}\left[\frac{\partial S[\phi]}{\partial \phi} P(\phi,\theta) + \frac{\partial P(\phi,\theta)}{\partial \phi}\right] = 0. \tag{2.61}$$

We can impose as a boundary term for the term in square brackets (the "probability flux") to vanish at infinity. Since it is constant, it also vanishes everywhere else. Then

$$\frac{\partial S[\phi]}{\partial \phi} P(\phi,\theta) + \frac{\partial P(\phi,\theta)}{\partial \phi} = 0 \tag{2.62}$$

is solved by

$$P(\phi) \propto e^{-S[\phi]}. \tag{2.63}$$

Thus, the Langevin equation in equilibrium samples from the PDF given by $e^{-S[\phi]}$. Observables may be calculated as

$$\langle O \rangle = \int_{\theta_{eq}}^{\infty} d\theta O(\phi(\theta)) \tag{2.64}$$

where θ_{eq} is the time the Langevin dynamics need to reach the stationary distribution. Using the discretized eq. (2.59), the integral is replaced by a sum

$$\langle O \rangle = \frac{\Delta\theta}{\theta_f - \theta_{eq}} \sum_{\theta=\theta_{eq}}^{\theta_f} O(\phi(\theta)) \tag{2.65}$$

which is the same as for the calculation of Monte Carlo expectation values. This makes the Langevin equation a Monte Carlo scheme.

Complexification

The complexification of the Langevin equation was first suggested in the 1980s by Parisi and Klauder [25], after the completion of the stochastic quantization program [26], with limited success in applications due to its problems discussed further below. Since some of the problems have now been solved, and computing resources increased, it has seen a resurgence.

For a complex action and a real field, the Langevin equation (eq. (2.58)) cannot be used, since the drift term is complex while the field is real. Even for complex fields, the update is not well defined, since $S[\phi]$ will usually not be holomorphic and contain terms such as $\phi^*\phi$,

so that the Wirtinger derivative cannot be taken. Complex Langevin solves this problem by complexifying the fields, doubling the degrees of freedom; A real field will then have two components, $\phi = \phi_R + i\phi_I$. The Langevin equation reads

$$\frac{\partial \phi_R}{\partial \theta} = -\mathrm{Re}\frac{\delta S}{\delta \phi_R} + \eta \tag{2.66}$$

$$\frac{\partial \phi_I}{\partial \theta} = -\mathrm{Im}\frac{\delta S}{\delta \phi_I}. \tag{2.67}$$

The noise term can theoretically be spread between real and imaginary update, but it almost always benefits stability if it is purely real [27], a notable exception being real time dynamics on Schwinger-Keldysh contours [9].
The corresponding Fokker-Planck equation reads

$$\begin{aligned}\frac{\partial P(\phi_R, \phi_I, \theta)}{\partial \theta} =& \frac{\partial}{\partial \phi_R}\left[\mathrm{Re}\left(\frac{\partial S[\phi]}{\partial \phi}\right) P(\phi, \theta)\right] + \frac{\partial^2 P(\phi, \theta)}{\partial \phi_R^2} \\ &+ \frac{\partial}{\partial \phi_I}\left[\mathrm{Im}\left(\frac{\partial S[\phi]}{\partial \phi}\right) P(\phi, \theta)\right].\end{aligned} \tag{2.68}$$

For observables that admit the extension $O(\phi) \to O(\phi_R + i\phi_I)$, it can, under mild assumptions, be shown [28] that there exists a complex function $\rho(\phi)$ satisfying

$$\int D\phi_I D\phi_R O(\phi_R + i\phi_I) P(\phi_R, \phi_I) = \int D\phi O(\phi)\rho(\phi). \tag{2.69}$$

The complex function $\rho(\phi)$ formally obeys the Fokker-Planck equation (eq. (2.61)). Therefore, we can calculate observables in the form

$$\langle O \rangle = \int D\phi_I D\phi_R O(\phi_R + i\phi_I) P(\phi_R, \phi_I) \tag{2.70}$$

from a real PDF $P(\phi_R, \phi_I)$. Since $\rho(\phi)$ follows the same Fokker-Planck equation as a real $P(\phi)$ would in case of a real PDF, we can interpret it as the "complex PDF" corresponding to the complex action $S(\phi)$, The Langevin process (eq. (2.67)) therefore samples from $P(\phi_R, \phi_I)$ and we infer that

$$\langle O \rangle = \int D\phi O(\phi) e^{-S[\phi]} \tag{2.71}$$

$$= \int D\phi O(\phi)\rho(\phi) \tag{2.72}$$

$$= \int D\phi_R D\phi_I O(\phi_R + i\phi_I) P(\phi_R, \phi_I) \tag{2.73}$$

$$= \int_0^\infty d\theta O(\phi_R(\theta) + i\phi_I(\theta)). \tag{2.74}$$

For a complex field $\psi = \phi + i\xi$, both ϕ and ξ are complexified, yielding four total components. The updates for all four variables ϕ_R,ϕ_I,ξ_R,ξ_I look like eq. (2.67). An alternative formulation for complex scalar fields is treating ψ and its conjugate ψ^* as independent. This is completely equivalent, since even in the previous formulation $\psi = \phi + i\xi \Rightarrow \psi^* = \phi - i\xi$ does not hold anymore. We call the "independent conjugate" variables ψ and $\bar{\psi}$, while marking "real conjugate" variables with a star *. Since most actions break holomorphy by using conjugates, instead of equivalently using the real and imaginary functions, the independent conjugate formulation is usually more convenient. Its updates simply read

$$\frac{\partial \psi}{\partial \theta} = -\frac{\delta S}{\delta \bar{\psi}} + \eta \tag{2.75}$$

$$\frac{\partial \bar{\psi}}{\partial \theta} = -\frac{\delta S}{\delta \psi} + \eta^* \tag{2.76}$$

where η is now a complex noise with real and imaginary part both being Gaussian white noise. Using the conjugate noise in eq. (2.76) is equivalent to the noise in eq. (2.67) being purely real. These updates are well defined, since S is now holomorphic in the complexified variables.

2.2.5 Limitations

The above derivation skips over a lot of mathematical intricacies, and therefore hides that the theory of Complex Langevin is not worked out completely. Specifically uniqueness and well-definedness of the stochastic process has not been shown. Neither do we know whether the process will converge towards an equilibrium measure. These issues have already been remarked by Klauder and Petersen in 1985 [29], and mostly remain unsolved. However, in practice, this does not seem to pose an issue, and rather practical problems become relevant.

Instability

Already early on, it was noted that the CL equations may permit trajectories for ϕ that reach infinity in finite time. While these are usually zero measure, these runaways still pose a practical problem in the implementation of CL simulations, leading to the process to diverge, or assume highly incorrect values. With increased computing power, it was noticed that these runaways are apparently caused by a coarse discretization in Langevin time. Today, almost all implementations of CL mitigate this using an *adaptive time step* [30]. It varies the time step depending on the maximum of the drift, usually in the form of

$$\Delta\theta = \Delta\theta_0 \times \frac{\langle \max_x \frac{\partial S}{\partial \psi} \rangle}{\max_x \frac{\partial S}{\partial \psi}}. \tag{2.77}$$

This shrinks the time step when the system comes close to a runaway trajectory, preventing a drift into unphysical regions for simple numerical reasons. The mean value of the drift is either known beforehand, found during equilibration, or kept as a running average. Runaways may still happen for extremely unstable systems, if the drift doesn't stop increasing.

Incorrect Convergence

While runaways are an issue easily noticed, another problem of the CL method is that the solution is not guaranteed to be correct. This is mainly caused by boundary conditions at infinity and poles in the probability distribution, which are assumed to not play a role during the derivation of the CL process. It is hard to know a priori if the correct values can be obtained, but a posteriori, there exist methods to verify the results. Specifically, in [31], it is shown that if the probability distribution of the drift term $P(\frac{\partial S}{\partial \psi})$ is suppressed exponentially at large ψ, then the CL method has converged to the correct value. We can easily save the drift size values and plot their histogram after a simulation. If the histogram is exponentially decaying, then the CL method converged towards the correct value. For the systems reviewed in this thesis, we usually do not have convergence issues.

Fundamental Limitations

In general, the complex Langevin method is more likely to fail the larger the complex part of the PDF becomes. This is seen in its extreme by the difficulties of even short real time simulations. It can be shown that NP-hard problems can be mapped onto quantum mechanical systems with a sign problem [32], so a generally efficient method of evading the sign problem would mean $P = NP$, that all problems of nondeterministic-polynomial complexity could actually be solved in polynomial time. Also, intuitively, it should not be possible to solve every quantum system efficiently. Since the physical quantum Hilbert space dimension scales exponentially in the number of particles, any method that can still efficiently sample from it might be considered a trick, making use of some symmetry of the problem to limit the amount of states to be considered. For systems with too large of a sign problem, there is no way around finding new ways to efficiently sample and approximate them, or eventually going beyond classical computing with quantum algorithms [33].

2.3 Theory of the Spin-1 Bose Gas

2.3.1 Low Energy Scattering Theory of the Spin-1 Gas

In the following, we derive the theory of low energy scattering of the spin-1 gas, summarized from Ho [34].
Since the creation of the first Bose-Einstein Condensate (BEC) using a magnetic trap, it

has been made possible to trap ultracold gases using purely optical means, preserving their hyperfine spin structure. In this thesis, we specifically consider gases with hyperfine spin $f = 1$, such as ^{23}Na, ^{39}K and ^{87}Rb. For spinor gases, there are multiple scattering channels allowed. Due to their symmetry, colliding bosons need to have total spin of either 0 or 2, leading to a total of two scattering lengths, a_0 and a_2, which describe the s-wave scattering behavior. The interaction is then well approximated by a contact potential

$$V(r_1 - r_2) = \delta(r_1 - r_2)(g_0\mathcal{P}_0 + g_2\mathcal{P}_2) \tag{2.78}$$

with $g_i = 4\pi a_i/M$. $\mathcal{P}_F$ is the projection operator onto the total spin F state. We may define the spin vector from the wavefunction

$$\mathbf{F}^\nu = \psi_a^\dagger(x)\sigma_{ab}^\nu\psi_b(x) \tag{2.79}$$

where σ_ν are the Pauli matrices in the Spin-1 representation

$$\sigma_x = \begin{pmatrix} 0 & 1 & 0 \\ 1 & 0 & 1 \\ 0 & 1 & 0 \end{pmatrix}, \sigma_y = i\begin{pmatrix} 0 & -1 & 0 \\ 1 & 0 & -1 \\ 0 & 1 & 0 \end{pmatrix}, \sigma_z = \begin{pmatrix} 1 & 0 & 0 \\ 0 & 0 & 0 \\ 0 & 0 & -1 \end{pmatrix}. \tag{2.80}$$

We know the relations

$$\mathbf{F}_1 \cdot \mathbf{F}_2 = \sum_{F=0}^{2f} \frac{1}{2}[F(F+1) - f(f+1)]\mathcal{P}_F \tag{2.81}$$

and

$$\mathbb{1} = \sum_F^{2f} \mathcal{P}_F \tag{2.82}$$

or, for $f = 1$ specifically

$$\mathbf{F}_1 \cdot \mathbf{F}_2 = \mathcal{P}_2 - 2\mathcal{P}_0 \tag{2.83}$$

$$\mathbb{1} = \mathcal{P}_2 + \mathcal{P}_2. \tag{2.84}$$

With this, we can rewrite the potential (eq. (2.78)) in the form

$$V(r_1 - r_2) = \delta(r_1 - r_2)[c_0\mathbb{1} + c_1\mathbf{F}_1 \cdot \mathbf{F}_2]. \tag{2.85}$$

The interaction Hamiltonian in the second quantized form then becomes

$$\hat{H}_{\text{int}} = -\frac{c_0}{2}\psi_a^\dagger\psi_b^\dagger\psi_b\psi_a - \frac{c_1}{2}\psi_{a'}^\dagger\psi_a^\dagger\sigma_{ab}^\nu\sigma_{a'b'}^\nu\psi_b\psi_{b'}. \tag{2.86}$$

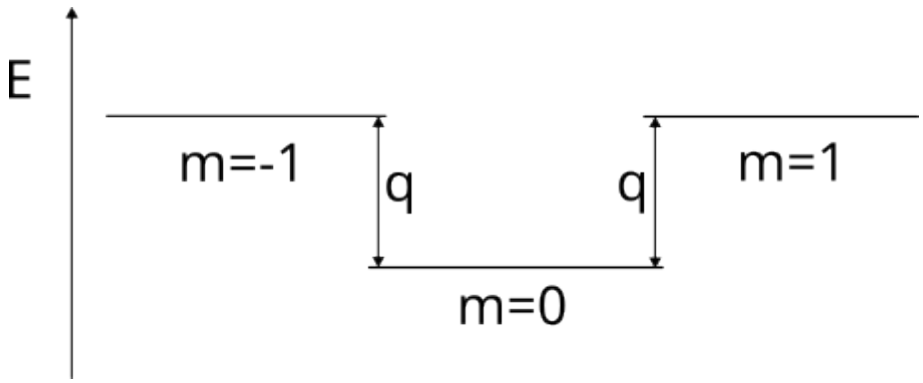

Figure 2.3: The quadratic Zeeman effect shifts the energy of the ±1 energy levels.

with spin interaction and density interaction constants

$$c_1 = \frac{g_0 + 2g_2}{3} \tag{2.87}$$

$$c_0 = \frac{g_2 - g_0}{3} \tag{2.88}$$

The interaction term proportional to c_0 describes spin preserving collisions, where particles emerge with the same spin they started in. It is spin independent, and may be rewritten as the $O(N)$ interaction

$$H_{\text{density}} = \frac{c_0}{2}|n|^2 \tag{2.89}$$

with density $n_i = \psi_i^\dagger \psi_i$. The spin changing interaction describes collisions where total spin is preserved, but the individual particles may change their state, i.e. a $f_1 = -1, f_2 = 1 \rightarrow f_1 = 0, f_2 = 0$ collision. It can be written as

$$H_{\text{spin}} = \frac{c_1}{2}|F|^2 \tag{2.90}$$

with spin density $F_\nu = \psi_a^\dagger \sigma_{ab}^\nu \psi_b$.
The non-interacting Hamiltonian is given by[35]

$$\hat{H}_0 = \sum_{m=-1}^{1} \frac{1}{2M} \nabla\psi_m^\dagger \nabla\psi_m - \mu\psi_m^\dagger\psi_m + qm^2\psi_m^\dagger\psi_m \tag{2.91}$$

with particle mass M, chemical potential μ and quadratic Zeeman effect q. The Zeeman effect is the result of an external magnetic field shifting the energy levels of the magnetized hyperfine states. It has a linear and quadratic order, i.e. $H_{Ze} = pm\psi_m^\dagger\psi_m + qm^2\psi_m^\dagger\psi_m$. The linear Zeeman effect shifts the $+1$ and -1 states in different directions, while the quadratic one shifts them the same way, upwards or downwards in energy. In low energy scattering, the total magnetization of the condensate is preserved during collisions. Therefore, the mean field population difference between the $+1$ and -1 states caused by a linear Zeeman

effect can be ignored. The remaining energy level shift leads to phase rotations in the -1 and 1 component, which can be included by shifting to the phase rotating frame [36]. This way, although the linear Zeeman shift is much larger than the quadratic one, it does not need to be included in the Hamiltonian.
The most important dimensionless quantity in the BEC is the diluteness

$$\eta = \sqrt{\rho a^3}. \tag{2.92}$$

If we interpret a^3 as the space taken up by one particle, then η describes the fraction of space filled with particles. As $\eta \to 1$, the theory becomes non-perturbative. When the diluteness is small enough, many beyond mean field corrections can be expressed as a power series in η, such as the shift of the critical temperature [37]. For the spin-1 gas, there are two diluteness parameters for the two available scattering lengths. This allows for interesting systems which are dense in density but dilute in spin density. The analytic expansion of quantum corrections in these dilutenesses is out of scope for this thesis.

2.3.2 Mean Field Theory

We describe the mean field theory of the spin-1 Bose gas, adapting from Kawaguchi and Ueda [35]. In zeroth order mean field theory, we consider the field $\psi(x)$ and Hamiltonian H to be classical, and simply find the state $\psi(x)$ that minimizes H. Without an external potential, this leads to a constant three component vector, which we call the mean field ground state. The influence of both spin changing collisions and the quadratic Zeeman effect leads to a rich zero temperature phase diagram of the condensate. The full diagram can be seen in fig. 2.4. It contains four main phases, determined by the parameters c_1 and q. When both $c_1 < 0$ and $q < 0$, c_1 favors the condensate being polarized, and q favors it being in the $m = \pm 1$ states. This leads to the *ferromagnetic* phase F, where the system spontaneously chooses a ground state $\psi = \begin{pmatrix} 1 \\ 0 \\ 0 \end{pmatrix}$ or $\psi = \begin{pmatrix} 0 \\ 0 \\ 1 \end{pmatrix}$. It is then polarized fully in the z direction, i.e. the direction of the magnetic field[4].
When $c_1 > 0$ and $q < 0$, the system favors being unpolarized in the ± 1 states. This leads to the *antiferromagnetic* phase AF, where the system is in the ground state $\psi = \begin{pmatrix} \frac{1}{\sqrt{2}} \\ 0 \\ \frac{1}{\sqrt{2}} \end{pmatrix}$.
If instead $q > 0$ and $c_1 > 0$, the system is in the *polar* phase P with $\psi = \begin{pmatrix} 0 \\ 1 \\ 0 \end{pmatrix}$. In both of these phases, the total magnetization of the condensate is zero.

[4] Using only magnetization preserving collisions, this ground state cannot be reached, and instead large domains of positive and negative magnetization in space will form [39].

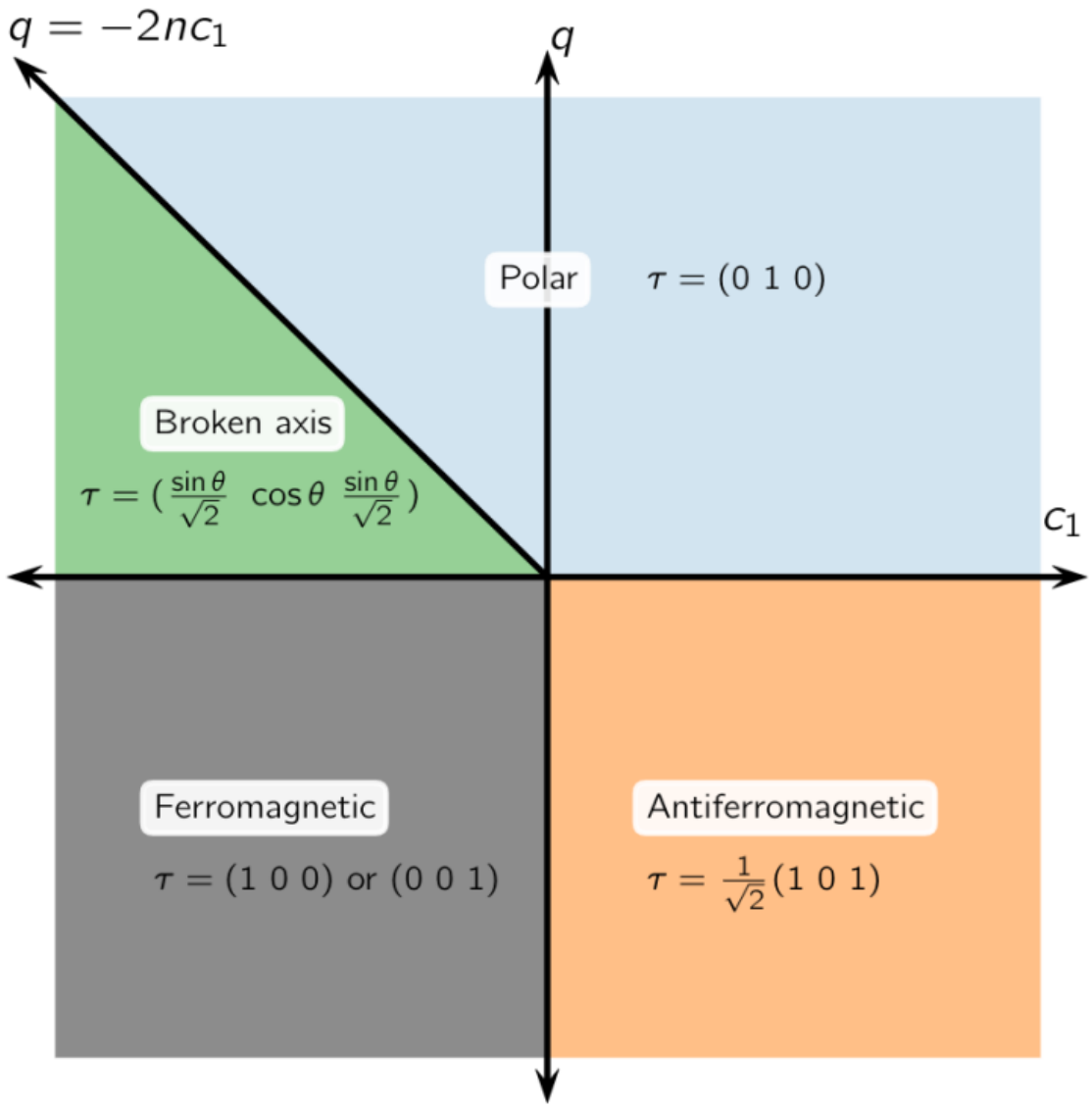

Figure 2.4: The phase diagram of the spin-1 Bose gas at zero temperature, adapted from [38]. The broken-axisymmetric (BA) phase is also called the easy-plane (EP) phase. θ is given by $\sin\theta = \sqrt{1/2 + 1/(4nc_1)}$

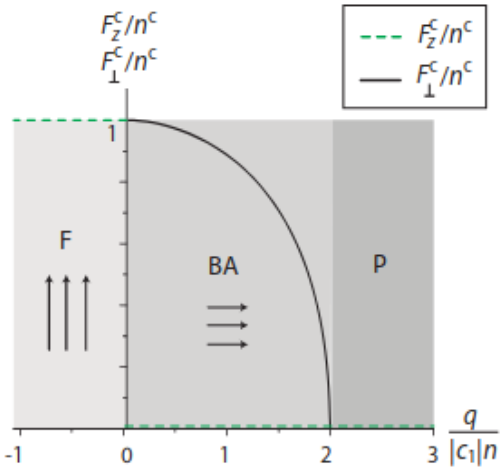

Figure 2.5: The finite temperature phase diagram of the ferromagnetic spin-1 Bose gas, adapted from [40]. In the BA phase, there is a two step condensation.

The most region of our interest in the phase diagram is reached when $q > 0$ and $c_1 < 0$, i.e. c_1 favors being polarized, but q favors the $m = 0$ sublevel. If $q > 2nc_1$, with density n, the Zeeman effect dominates, and the system remains in the polar phase P. However, for $q < 2nc_1$, the system polarizes perpendicularly to the magnetic field, and spontaneously chooses a magnetization in the XY plane. This is called the *Easy Plane* phase EP, with ground state $\psi = \begin{pmatrix} \frac{\sqrt{1-\bar{q}}}{2} \\ \sqrt{\frac{1+\bar{q}}{2}} \\ \frac{\sqrt{1-\bar{q}}}{2} \end{pmatrix}$, $\bar{q} = -q/(2nc_1)$. The system is partially polarized, now in the XY plane, with total magnetization $F_\perp = \sqrt{1-\bar{q}^2}$.

2.3.3 Finite Temperature

The finite temperature phase diagram of a Bose gas usually consists of a normal, disordered phase, and a condensed BEC phase. The same is the case for the spinor Bose gas. Its condensation temperature is generally lower due to multiple particle species, with $T_{c1} = (\frac{1}{3})^{\frac{2}{3}}$ for the O(N) gas [40]. In the broken-axisymmetric phase, there is the additional feature of two step condensation (fig. 2.5). In the EP ground state, all hyperfine sublevels are macroscopically occupied, but, due to the quadratic Zeeman effect, have a different effective chemical potential. This means that the sublevel $m = 0$ condenses first, at temperature T_{c1}, equal to the critical temperature for the O(N) gas $(\frac{1}{3})^{\frac{2}{3}} T_{c0}$. The system is then in the polar phase, with the $m = 0$ state condensed and $m = \pm 1$ only thermally occupied. At a lower temperature T_{c2}, the $m = \pm 1$ states condense as well, and the system enters the EP phase. This critical temperature T_{c2} is dependent on q and nontrivial to determine. We calculate the polar-EP phase boundary in an exact way using complex Langevin in section 4.7.

2.3.4 Bogoliubov Theory

To gain analytical insight into ultracold gases, we employ Bogoliubov Theory. We summarize here results from Wen [3] and Phuc, Kawaguchi, and Ueda [40]. It involves the application of a *Bogoliubov transformation* to transform the creation and annihilation operators $a^\dagger$ and a to quasiparticle operators $b^\dagger$ and b. As the simplest example of Bogoliubov theory, we first consider the Fock space Hamiltonian of an interacting single component Bose gas

$$H = \int_x \phi^\dagger(x)(\frac{\nabla^2}{2m} - \mu)\phi(x) + \int_x \int_y V(x,y)\phi^\dagger(x)\phi^\dagger(y)\phi(y)\phi(x) \tag{2.93}$$

or in momentum space with $\epsilon_k = \frac{k^2}{2m}$

$$H = \sum_k (\epsilon_k - \mu) a_k^\dagger a_k + \sum_{k,k',q} V_q a_{k-q}^\dagger a_{k'+q}^\dagger a_{k'} a_k. \tag{2.94}$$

This Hamiltonian is non-diagonal, since the first term couples different locations in real space, and the second term couples different momenta in momentum space. In a BEC, the $k = 0$ mode is macroscopically occupied, while the other modes are assumed to be only sparsely occupied. Letting $|\phi\rangle$ be a BEC state, the approximation $a_0 |\phi\rangle \approx a_0^\dagger |\phi\rangle \approx \sqrt{N_0} |\phi\rangle$ is therefore valid. One can insert this approximation and expand to order N_0, leaving the ground state energy GSE as an arbitrary shift

$$H = GSE + \sum_k (\epsilon_k - \mu + \rho_0 V_0 + \rho_0 V_k) + \frac{1}{2}\rho_0 \sum_k V_k (a_{-k} a_k + a_k^\dagger a_{-k}^\dagger). \tag{2.95}$$

To diagonalize this Hamiltonian, we write it in matrix form

$$H = GSE + \sum_{k \neq 0} \begin{pmatrix} a_k^\dagger & a_{-k} \end{pmatrix} \begin{pmatrix} L_k & M_k \\ M_k & L_k \end{pmatrix} \begin{pmatrix} a_k \\ a_{-k}^\dagger \end{pmatrix}. \tag{2.96}$$

with

$$L_k = (\epsilon_k - \mu + \rho_0 V_0 + \rho_0 V_k) \tag{2.97}$$

$$M_k = \rho_0 V_k. \tag{2.98}$$

The transformation we are looking for is the symplectic transform

$$\begin{pmatrix} a_k \\ a_{-k}^\dagger \end{pmatrix} = U(k) \begin{pmatrix} b_k \\ b_{-k}^\dagger \end{pmatrix} \tag{2.99}$$

that diagonalizes the matrix in eq. (2.96) and preserves the commutation relations $[a_k^\dagger, a_{k'}] = [b_k^\dagger, b_{k'}] = 1$. Such a transform is given by a matrix [41]

$$U(k) = \begin{pmatrix} u_k & v_k^* \\ -v_k & -u_k^* \end{pmatrix} \tag{2.100}$$

with $|u_k|^2 - |v_k|^2 = 1$. The transform is then

$$a_k = u_k b_k - v_k^* b_{-k}^\dagger. \tag{2.101}$$

More generally, a there might be multiple particle species, like the three spin states in a spin-1 gas, with nontrivial interactions. Nevertheless, we can always write the interacting Hamiltonian (expanded to second order) in the form

$$H_{\text{int}} = \sum_{k=0} a_i^{k\dagger} A_{ij}^k a_j^k + \frac{1}{2}(a_i^{k\dagger} B_{ij}^k a_j^{k\dagger} + a_i^k B_{ij}^{k*} a_j^k) \tag{2.102}$$

with i, j running over the N particle species. The Bogoliubov-de Gennes eigenvalue equations are given for each k as

$$\begin{pmatrix} A_{ij} & B_{ij} \\ -B_{ij}^* & -A_{ij}^* \end{pmatrix} \begin{pmatrix} u_j \\ v_j \end{pmatrix} = \epsilon \begin{pmatrix} u_i \\ v_i \end{pmatrix} \tag{2.103}$$

with normalization condition

$$\sum_i (|u_i|^2 - |v_i|^2) = 1 \tag{2.104}$$

There are 2N possible solution to the block-matrix equation, with only the positive eigenvalues $\epsilon > 0$ being physical solutions. We introduce the transformation matrices $U_{ij} = (u_i)_j$, $V_{ij} = (v_i)_j$. The transformation from quasiparticles to real particles is then given by

$$A_k = U_k B_k - V_k B_k^\dagger \tag{2.105}$$

where $B_K = \begin{pmatrix} b_{1,k} \\ b_{2,k} \\ \dots \end{pmatrix}$, $A_K = \begin{pmatrix} a_{1,k} \\ a_{2,k} \\ \dots \end{pmatrix}$.

2.3.5 Bogoliubov Observables

The Bogoliubov approximation allows for an easy way to calculate the quantum depletion of the condensate. The quasiparticle vacuum is given by the relation

$$b_i |\Omega\rangle = 0 \tag{2.106}$$

for each mode i. In the quasiparticle ground state, real particles can still be excited.To find their occupation numbers, consider the particle basis operators acting on the quasiparticle vaccum state [40]

$$F_{\text{quant}}(k) = \langle\Omega|A_k^\dagger A_k|\Omega\rangle \tag{2.107}$$
$$= \langle\Omega|\, B_k^\dagger U_k^\dagger U_k B_k + B_{-k}V_k^\dagger V_k B_{-k}^\dagger + B_k^\dagger U_k V_k^\dagger B_{-k}^\dagger + B_{-k}V_k U_k^\dagger B_k\,|\Omega\rangle \tag{2.108}$$
$$= \text{Tr}(V_k^\dagger V_k). \tag{2.109}$$

Other vacuum observables may be calculated in a similar fashion.
For thermal observables, one can use the Bose-Einstein distribution

$$\langle T|b_{i,k}^\dagger b_{i,k}|T\rangle = \frac{1}{e^{\beta\omega_i(k)}-1} \tag{2.110}$$

for thermal state $|T\rangle$ and $\beta = 1/T$. Since the quasiparticles are also bosonic, one can read off their dispersion from the diagonalized Hamiltonian, which has the form $H = \sum_k \omega(k) b_k^\dagger b_k$. We may replace the vacuum state $|\Omega\rangle$ in eq. (2.107) with a thermal state $|T\rangle$ and find

$$F(k) = F_{\text{therm}}(k) + F_{\text{quant}}(k) \tag{2.111}$$
$$= \text{Tr}(U_k^\dagger U_k T_k) + \text{Tr}(V_k^\dagger V_k T_k) + \text{Tr}(V_k^\dagger V_k) \tag{2.112}$$

with matrix $T_k = diag\left(\frac{1}{e^{\beta\omega_1(k)}-1}, \frac{1}{e^{\beta\omega_2(k)}-1}, \dots\right)$. Again, other observables may also be calculated using the presented method.

2.3.6 Bogoliubov Theory of the Spin-1 Bose Gas

For the Spin-1 Bose Gas, the Bogoliubov transformations necessary depend on the phase of the system. The full transformations for all phases are given in [41]. For completeness, we give the transformations for the easy-plane phase, which is the one that is mostly examined in this thesis. We later use a more involved, numerical Bogoliubov ansatz for the finite temperature phase diagram [40].
We first perform a basis change of particle operators

$$\hat{a}_{\mathbf{k},d} = \frac{\sin\theta}{\sqrt{2}}\left(\hat{a}_{\mathbf{k},1} + \hat{a}_{\mathbf{k},-1}\right) + \cos\theta\hat{a}_{\mathbf{k},0} \tag{2.113}$$
$$\hat{a}_{\mathbf{k},f_z} = \frac{1}{\sqrt{2}}\left(\hat{a}_{\mathbf{k},1} - \hat{a}_{\mathbf{k},-1}\right) \tag{2.114}$$
$$\hat{a}_{\mathbf{k},\theta} = \frac{\cos\theta}{\sqrt{2}}\left(\hat{a}_{\mathbf{k},1} + \hat{a}_{\mathbf{k},-1}\right) - \sin\theta\hat{a}_{\mathbf{k},0} \tag{2.115}$$

with $\sin\theta = \sqrt{1/2 + 1/(4nc_1)}$. We define

$$E_{\mathbf{k},f_z} = \sqrt{\epsilon_{\mathbf{k}}\left(\epsilon_{\mathbf{k}} + q\right)} \tag{2.116}$$

$$E_{\mathrm{k},\pm} = \sqrt{\epsilon_{\mathrm{k}}^2 + n\left(c_0^{(1)} - c_1^{(1)}\right)\epsilon_{\mathrm{k}} + 2n^2 c_1^{(1)}\left(c_1^{(1)} - c_q^{(1)}\right) \pm E_1(k)} \tag{2.117}$$

$$X_{1\pm}(k) = -n\left(c_0^{(1)} + 3c_1^{(1)} - 2c_q^{(1)}\right)\epsilon_{\mathbf{k}} + 2n^2 c_1^{(1)}\left(c_1^{(1)} - c_q^{(1)}\right) \pm E_1(k) \tag{2.118}$$

$$\begin{aligned} E_1(k) = \Bigg\{ &\left[\left(n^2\left(c_0^{(1)} + 3c_1^{(1)}\right)^2 - 4n^2 c_q^{(1)}\left(c_0^{(1)} + 2c_1^{(1)}\right)\right]\epsilon_{\mathbf{k}}^2 - 4n^3 c_1^{(1)}\left(c_0^{(1)} + 3c_1^{(1)}\right)\left(c_1^{(1)} - c_q^{(1)}\right)\epsilon_{\mathbf{k}} \\ &+ \left[2n^2 c_1^{(1)}\left(c_1^{(1)} - c_q^{(1)}\right)\right]^2\Bigg\}^{1/2} \end{aligned} \tag{2.119}$$

$$C_{1\pm}(k) = \frac{E_{\mathbf{k}\pm}}{X_{1\mp}^2(k)\epsilon_{\mathbf{k}} + q^2\epsilon_{\mathbf{k}}^2\left(\epsilon_{\mathbf{k}} - 2nc_1^{(1)}\right)\sin^2 2\theta} \tag{2.120}$$

The full transformation matrices are given as

$$U(k) = \frac{1}{2}\begin{pmatrix} \sqrt{\frac{\epsilon_{\mathbf{k}}+q/2+E_{\mathbf{k},f_2}}{2E_{\mathbf{k},f_2}}} & 0 & 0 \\ 0 & \frac{1}{2C_1(k)E_1(k)} + C_{1-}(k)X_{1+}(k) & q\epsilon_{\mathbf{k}}C_{1-}(k)\sin 2\theta - \frac{X_1-(k)}{2q\epsilon_k C_1-(k)E_1(k)\sin 2\theta} \\ 0 & -\frac{1}{2C_{1+}(k)E_1(k)} + C_{1+}(k)X_{1-}(k) & q\epsilon_{\mathbf{k}}C_{1+}(k)\sin 2\theta + \frac{X_1(k)}{2q\epsilon_k C_{1+}(k)E_1(k)\sin 2\theta} \end{pmatrix} \tag{2.121}$$

$$V(k) = \frac{1}{2}\begin{pmatrix} \sqrt{\frac{\epsilon_{\mathbf{k}}+q/2-E_{\mathbf{k},f_2}}{2E_{\mathbf{k},f_2}}} & 0 & 0 \\ 0 & -\frac{1}{2C_1-(k)E_1(k)} + C_{1-}(k)X_{1+}(k) & q\epsilon_k C_{1-}(k)\sin 2\theta + \frac{X_1-(k)}{2q\epsilon_k C_1-(k)E_1(k)\sin 2\theta} \\ 0 & \frac{1}{2C_1+(k)E_1(k)} + C_{1+}(k)X_{1-}(k) & -q\epsilon_k C_{1+}(k)\sin 2\theta - \frac{X_1(k)}{2q\epsilon_k C_1+(k)E_1(k)\sin 2\theta} \end{pmatrix} \tag{2.122}$$

For vectors $B_k = (b_z^k, b_+^k, b_-^k)$, $A_k = (a_{f_z}^k, a_d^k, a_\theta^k)$. The transform is then given by

$$B_k = U(k)A_k + V(k)A_k^\dagger \tag{2.123}$$

The dispersion of the modes is given by the energies eq. (2.116) and eq. (2.117). We show examples of thermal and quantum occupation in fig. 2.6.

2.3.7 Renormalization of parameters

In complex Langevin simulations, the parameters plugged into the simulation describe the physics at a microscopic level, the scale of the lattice spacing. However, at a macroscopic level, they are modified by quantum fluctuations. These *renormalized* parameters are what is measured in experiment, and for correct comparisons have to be calculated from the *bare* parameters supplied to the simulation. We show here how renormalization corrects the parameters supplied to complex Langevin simulations, following Heinen [42] and Phuc, Kawaguchi, and Ueda [40]

The renormalized parameters are given by a series expansion, with the expansion parameter being the bare coupling g. In the spin-1 gas, we have two coupling constants g_0 and g_2,

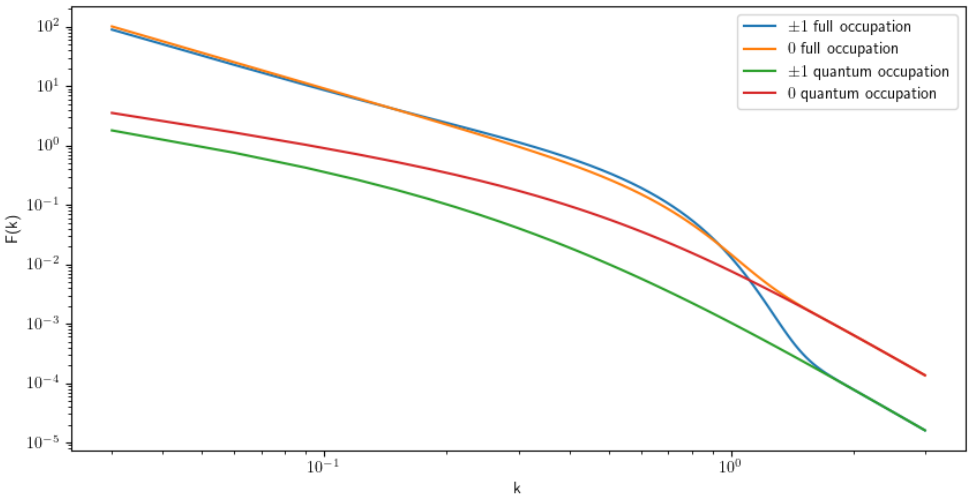

Figure 2.6: The full and quantum depletion of the condensate. Parameters given in 6.1

Figure 2.7: The first order correction and some higher order power series corrections to the coupling. These diagrams can be rewritten as a geometric series to infinite order

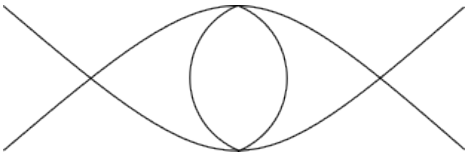

Figure 2.8: A higher order diagram not included in the infinite sum shown in fig. 2.7

given by eq. (2.88), which have to be renormalized individually, but independently [40]. We focus on the first order expansion, summarizing mostly [42]. The renormalized coupling reads

$$g = \tilde{g} - \frac{\tilde{g}^2}{\Omega} \sum_k \frac{1}{2\epsilon_k^0} \tag{2.124}$$

with bare coupling $\tilde{g}$ and renormalized coupling g. The energy is given by $\epsilon_k = \frac{k^2}{2M}$. Alternatively, by series inversion we can write

$$\tilde{g} = g + \frac{g^2}{\Omega} \sum_k \frac{1}{2\epsilon_k^0} \tag{2.125}$$

Typically, these sums are UV divergent in 3 dimensions, with renormalization "absorbing" the infinities. In lattice field theory, there is natural ultraviolet cutoff given by the length scale a_s. It is chosen much larger than the "problematic" scattering length a, where the theory becomes invalid. Therefore the sums only result in a finite correction proportional to a/a_s. Setting as a cutoff $\Lambda = \pi a_s^{-1}$ and evaluating the sum as a continuous integral

$$g = \tilde{g} - m\tilde{g}^2 \int_0^\Lambda \frac{d^3p}{(2\pi)^3} \frac{1}{p^2} = \tilde{g} - \frac{m\tilde{g}^2}{2\pi a_s} \tag{2.126}$$

results

$$\frac{\tilde{g} - g}{\tilde{g}} = 2\frac{a}{a_s} \tag{2.127}$$

For lattice simulations, the momenta are not being cut off on a circle, but instead component wise. Additionally, the momenta are separated by a finite distance depending on the extent of the lattice. To get the correct renormalization, we perform the momentum sum in eq. (2.124) numerically over the momentum grid used in the lattice simulation.
An additional factor influencing the renormalization is the finite lattice spacing in imaginary time direction. It produces a correction to the propagator, which can be incorporated into the renormalized coupling by writing [42]

$$g = \tilde{g} - \frac{\tilde{g}^2}{\Omega} \sum_k \frac{1}{2\epsilon_k} \frac{1}{1 - a_\tau \frac{k^2}{4M}} \tag{2.128}$$

This correction diverges when $a_\tau = \frac{4M}{k_{max}^2}$, and thus confirms the maximum stable momentum determined in eq. (4.11).
We find that one can get some higher order corrections without further calculations by looking at diagram summations (See fig. 2.7). The vertex+loop can be seen as a unit, giving the first order correction

$$g^{(1)} = -\frac{\tilde{g}}{\Omega} \sum_k \frac{1}{2\epsilon_k} \frac{1}{1 - a_\tau \frac{k^2}{4m}} \tag{2.129}$$

A higher order diagram is composed of one vertex and n vertex+loop combinations. This can be written as a geometric sum

$$g = \tilde{g}(1 + g^{(1)} + (g^{(1)})^2 + \ldots) = \frac{\tilde{g}}{1 - g^{(1)}} \tag{2.130}$$

This is similar to the one-particle-irreducible summations common in renormalization of propagators [2]. Obviously, at higher orders additional diagrams appear, like fig. 2.8. These would have to be calculated independently and are not included in the summation scheme. When comparing results from complex Langevin simulations to other, non-microscopic simulations or experiment, we should always compare to the renormalized parameters for the CL simulation to have a correct comparison.

2.4 Scaling at Phase Transitions

Classical phase transitions are characterized by a change in a materials macroscopical properties when varying the temperature, for example water freezing at 0°C, or a ferromagnet magnetizing at its Curie temperature [43]. In contrast, a quantum phase transition can by definition only happen at 0K [44]. It is then controlled not by temperature, but by an external parameter, like a magnetic field strength. We show that many properties which hold for classical phase transitions, in a similar way hold for quantum ones. For a more in-depth introduction, see Sachdev [44], which we mostly summarize.

2.4.1 Classical Phase Transitions

Classical phases are usually characterized by an order parameter, which is 0 above the critical temperature T_c (the *disordered phase*) and nonzero below T_c. If there is a sharp jump in the order parameter, the phase transition is called first order. In the case that the order parameter only has a kink at $T = T_c$, and the jump happens only in its derivative, the phase transition is called second order.
We now turn to the theory of scaling at phase transitions. From renormalization group theory, it can be shown that the system has to be scale invariant at a critical point. Therefore, its correlation length must become infinite. Close to a second order phase transition, the correlation length then diverges with a critical exponent ν [44]

$$\xi_c \propto |T - T_c|^{\nu} \tag{2.131}$$

This exponent is called *universal*, since it only depends on the macroscopic properties of the system, e.g. its symmetries, and not its microscopic parameters.
To analyze quantum phase transitions, we use the imaginary time formalism, describing a QFT at zero temperature as $d + 1$ dimensional. Close to a phase transition with critical

parameter q_c, we also find a diverging correlation length in imaginary time ξ_τ.

$$\xi_c \propto |q - q_c|^\nu \tag{2.132}$$

$$\xi_\tau \propto \xi_c^z \tag{2.133}$$

z is known as the dynamical critical exponent, also appearing in phenomena of critical slowing down.

The word quantum in quantum phase transitions can be misleading, since for Bose-Einstein condensation, quantum effects are needed to occur, yet the phase transition is classical. While quantum fluctuations control the microscopic physics, at scales $d \sim 1/T$ thermal fluctuations begin to dominate and control the macroscopic fluctuations. This is always true for any temperature except $T = 0$, at least while the volume is infinite. Quantum critical effects may still be observed experimentally, since the quantum critical point controls even finite temperature physics close to it.

2.4.2 Finite Temperature Regime

Sharp phase transitions only exist in the thermodynamic limit with $V \to \infty$. For quantum phase transitions, the same holds, but in $d + 1$ dimensions; the imaginary time extent has to be infinite. Therefore, finite temperature physics close to a quantum critical point corresponds to a finite-size imaginary time dimension. We encounter one of the scenarios described in fig. 2.9. The critical behavior of systems with finite extent is well known from classical phase transitions, and is described by the theory of finite-size scaling. In essence, it amounts to adding the inverse size of the system $1/L$ as a scaling variable to observables. In the case of a QPT, we have $L_\tau = \beta$, and observables scale as [45]

$$O(k, \omega, q, T) = \beta^{d_O/z} O(k\beta^{1/z}, \omega\beta, \beta/\xi_\tau) \tag{2.134}$$

Where d_O is the variables scaling dimension. This means that, in general, extrapolations can be done using a power law fit in T. Similarly, finite-size corrections in space also follow a power law in $1/L$.

The width of the phase transition also scales as $(\frac{1}{L})^{1/\nu}$[46]. However, finite-size scaling also provides a more accurate way of finding the transition, with a accuracy of $(\frac{1}{L})^{1/\nu+\omega}$, where ω is another critical exponent associated with the "irrelevant" corrections. This is done using the Binder cumulant [47]. We use here the definition

$$B = \frac{\langle O^4 \rangle}{\langle O^2 \rangle^2} \tag{2.135}$$

where O is the order parameter describing the phase transition. In the $V \to \infty$, $T \to 0$ limit, the cumulant makes a jump at a second order phase transition, while in the finite-size regime, there is a crossover. At the critical point, the cumulant must take a critical value B_c. Finite-

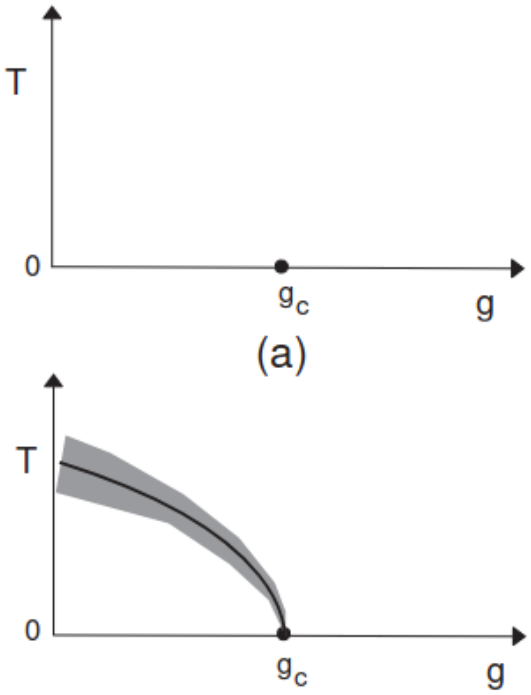

Figure 2.9: The two possibilities for the finite temperature behavior around quantum critical points. In the upper graph, the behavior at finite temperatures is completely analytic and described by scaling close to the critical point. In the lower graph the QCP is the end of a line of classical critical points, so that the shaded region is described by the theory of classical phase transitions. Close to the quantum critical point, additional quantum effects complement the classical behavior. Adapted from [44]

size scaling theory tells us that the first order finite-size corrections of the expectation values, proportional to $(\frac{1}{L})^{1/\nu}$, cancel each other [48]. Additionally, the value of the cumulant itself is universal, that is, it only depends on the type of system and not its exact parameters. We can therefore determine the critical parameter by simulating the system on two lattices of different size L_1^d and L_2^d, and determining the point where $B(L_1, q) = B(L_2, q)$. Additionally, since B_c is universal, once the value of the critical cumulant is known, the system only needs be simulated for one size, and the point $B(L, q) = B_c$ determined. This technique can be used both for finite and zero temperature phase transitions, by either increasing L only or both L and β.

Chapter 3

Complex Langevin Methods

3.1 Kernel Acceleration

As discussed in section 2.4, at phase transitions, the characteristic correlation length ξ_c of the system is not well described by mean field theory, and instead diverges with a critical exponent ν. In a finite-size system, this leads to a slowing down of the lattice dynamics. While updates of the lattice are local (except for the Laplacian), correlation at a phase transition spans the whole lattice. This increases the Monte Carlo autocorrelation time, and thus decreases the speed at which we gain statistics.
The simplest example for critical slowing down is seen in a free scalar field theory with momentum space Lagrangian

$$L_{free} = \frac{1}{2}\psi(p^2 + m^2)\psi \tag{3.1}$$

The relevant length scale is $\xi = \frac{1}{m}$. We see that the Langevin drift is given by

$$\frac{\partial S}{\partial \psi} = (p^2 + m^2)\psi \tag{3.2}$$

For small masses m, the evolution of high momenta is a lot faster compared to lower ones, with the slowing down becoming infinitely large at the phase transition point $m = 0$. However, the Langevin process naturally offers a way to alleviate this problem.

3.1.1 Kernel Freedom

As mentioned before, the stochastic process eq. (2.58)

$$\frac{d\phi(x)}{d\theta} = -\frac{\delta S[\phi]}{\delta \phi(x)} + \eta \tag{3.3}$$

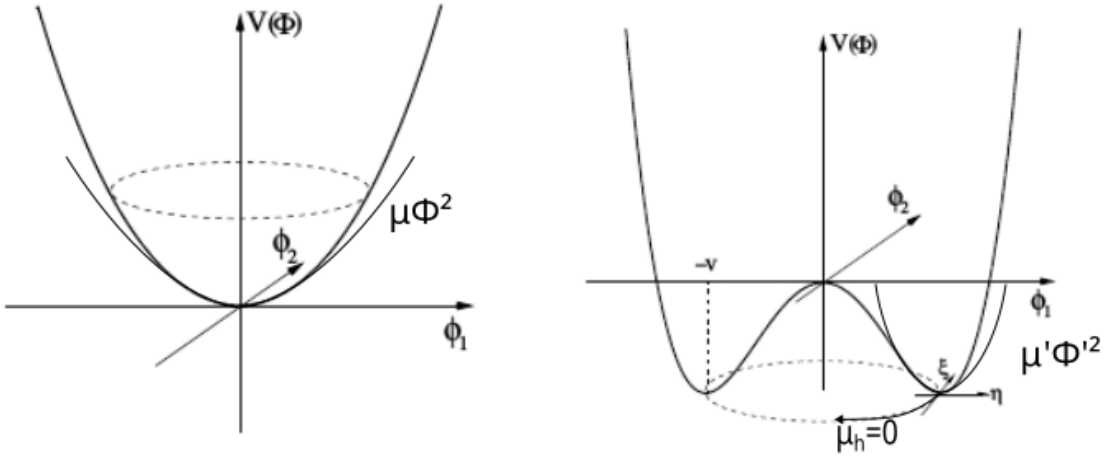

Figure 3.1: Free part of the potential without (left) and with (right) spontaneous symmetry breaking. The free part μ of the potential might be different when expanding from the new minimum. There is also be a massless Goldstone boson along the valley of the potential. Modified and adapted from [49]

corresponds to a Fokker Plank equation

$$\frac{\partial P(\phi,\theta)}{\partial \theta} = \frac{\partial}{\partial \phi}\left[\frac{\partial S[\phi]}{\partial \phi} P(\phi,\theta)\right] + \frac{\partial^2 P(\phi,\theta)}{\partial \phi^2}. \tag{3.4}$$

It can be shown that, more generally, we may add a positive definite matrix $K(x,y)$ [50][51], also known as a kernel, such that

$$\frac{d\phi(x)}{d\theta} = -K(x,y)\frac{\delta S[\phi]}{\delta \phi(y)} + \sqrt{K(x,y)}\eta(y). \tag{3.5}$$

The equilibrium distribution of the new Fokker Plank equation will be the same one as eq. (3.4). This fact is called *kernel freedom*. Returning to the example of the free scalar field (eq. (3.2)), we can introduce a kernel that is local in momentum space

$$K(p) = \frac{1}{p^2 + m^2}. \tag{3.6}$$

The Langevin drift is then

$$\frac{\partial S}{\partial \phi} = \frac{1}{p^2 + m^2}(p^2 + m^2)\phi = \phi \tag{3.7}$$

while the noise terms modified to

$$\sqrt{\frac{1}{p^2 + m^2}}\eta(p). \tag{3.8}$$

This completely eliminates critical slowing down from the Langevin process. For interacting fields, an exact kernel cannot be found, since the action is not local in momentum space. However, a kernel can anyway be constructed by considering just the free part of the action. We show that this still accelerates Langevin dynamics substantially, especially at phase transitions.

For the coherent state path integral, the free update in momentum space is given by eq. (4.9), such that the optimal kernel is given by

$$K(k) = \left| 1 - (1 - a_\tau \frac{k^2}{2M} + a_\tau \mu) e^{-2\pi i j / N_\tau} \right|^{-1}. \tag{3.9}$$

In theory, this is only stable for $\mu < 0$, since otherwise $K \to \infty$. However, in the symmetry broken phase, we have to replace μ by a new expansion parameter μ_{eff} which describes the quadratic behavior in the true vacuum. In theory, we have two components, one massless and one massive, see fig. 3.1. Since the decomposition would be dependent on the state of the system, this proves infeasible, and we therefore simply choose a μ_{eff} in the range $[1/L, \mu]$. While this cannot cancel critical slowing down to the same degree as in the unbroken theory, we still see a substantial speedup. In fig. 3.2, we show the autocorrelation Langevin time depending on momentum for a single component gas. One can see that without a kernel,

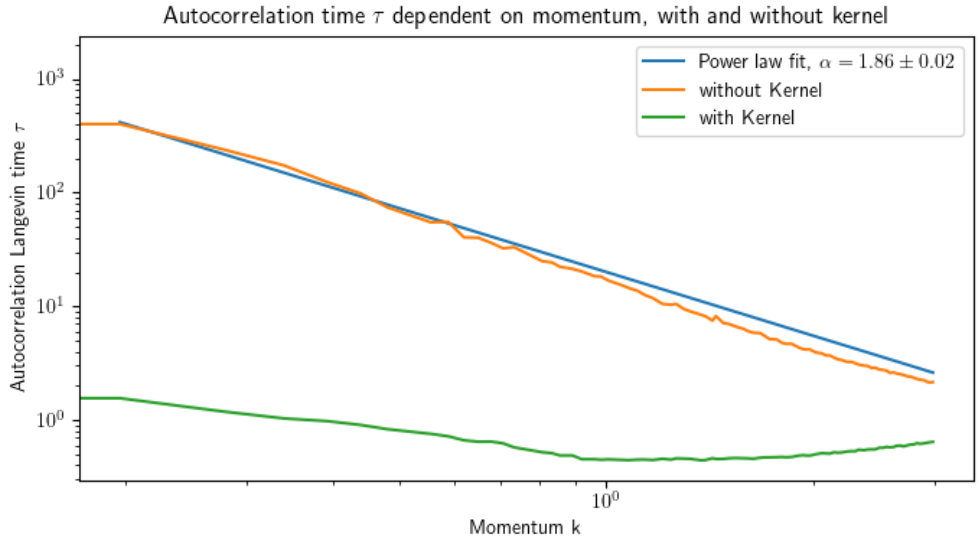

Figure 3.2: Autocorrelation time of the Langevin process depending on the momentum mode. The autocorrelation has been determined by fitting $f(t) = \exp(-\frac{t}{\tau})$ to the autocorrelation curve (fig. 3.3) for each lattice momentum k. For low momenta the process is accelerated by two orders of magnitude using a kernel. The curve is considerably flattened, resulting in a speed up of more than two orders of magnitude for low momenta. A power law fit to the unaccelerated autocorrelation time shows $\tau \sim k^{-1.86}$, justifying the assumption of a roughly quadratic behavior. Full parameters in appendix

the autocorrelation decays much slower for low momentum modes. In fig. 3.3 we specifically

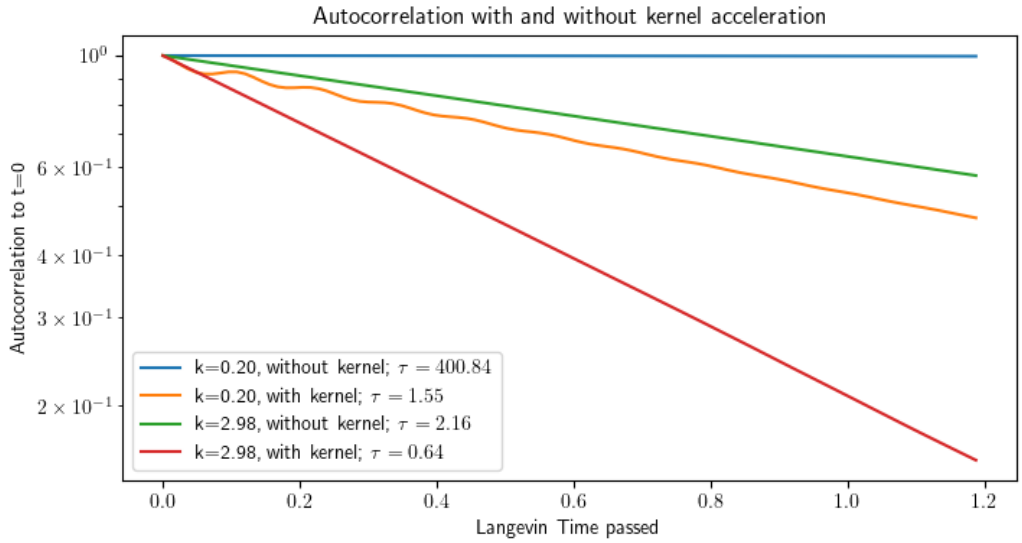

Figure 3.3: The autocorrelation with or without a kernel. The high momentum mode is accelerated slightly, the low one considerably. Autocorrelation time τ are obtained from fitting $f(t) = \exp(-\frac{t}{\tau})$.

visualize the difference for two modes. A possible problem of kernel acceleration might be introduction of bias, in the same way as bias is introduced for large time steps. We perform a comparative study for a specific parameter set between accelerated and non-accelerated simulations, and compare the resulting density $\rho = \int dx \psi\bar{\psi}$ and its standard deviation (fig. 3.4). Standard deviation is smaller for the accelerated simulations (as expected), and

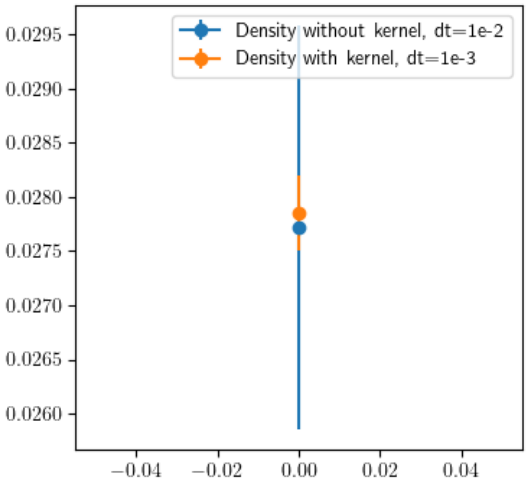

Figure 3.4: Comparison of the mean and standard deviation of the density with and without kernel acceleration. Both simulations were run 10 times each for 12 hours. While the accelerated dynamics outperforms in convergence by a big margin, the mean values are within one standard deviation of each other, showing no bias larger than statistical error.

the values correctly lie within the confidence interval of the kernel-free simulation, meaning the bias is lower than the statistical error typical for a 24h simulation. When performing a simulation with very high kernel acceleration, bias might still be introduced through the

noise when time steps are large. To prevent this, we keep the effective μ_{eff} reasonably high and the time step sufficiently low.
Lastly, kernel acceleration is only effective when a quadratic approximation is valid. If higher order terms in the interaction play a nonperturbative role, the accelerated dynamics might cause the simulation to diverge. We therefore only apply kernel acceleration to dilute systems with a diluteness (eq. (2.92)) $\eta \leq 10^{-3}$. A further topic of research might be to slow down the dynamics instead of accelerating them, to make simulations more stable and access higher diluteness regions.

3.2 Histogram Reweighting

Phase transitions in finite-size systems are not sharp, but instead smooth crossovers. One usually wants to scan the parameter regime around the transition with multiple Monte Carlo simulations, and then interpolate between the measurements to find the parameters of interest. The error of this procedure is directly dependent both on statistics for every single data point, as well as the parameter spacing between each simulation. For good statistics at a phase transition, using large lattices, typical simulation times are on the order of days (even with kernel acceleration and using high-end GPUs), so one would like to make the interpolation process as efficient as possible. In [52], Ferrenberg and Swendsen invented a data analysis technique for Monte Carlo sampling that is here adapted to complex Langevin: histogram reweighting.
As an example, consider the ϕ^4 action

$$S = \int d^d x [m\phi^2 + \lambda\phi^4] \tag{3.10}$$

The corresponding probability density function is

$$P(\phi) = \frac{e^{-S[\phi]}}{\int D\phi' e^{-S[\phi']}} \tag{3.11}$$

Suppose we have done Monte Carlo sampling to find an observable $O(\phi)$ for given values $m = m_0$, $\lambda = \lambda_0$. Given another value λ_1, we can relate the PDFs by

$$P_{\lambda_1}(\phi) = P_{\lambda_0}(\phi) e^{\int d^d x(\lambda_0 - \lambda_1)\phi^4} \frac{\int D\phi' e^{-S[\phi']}}{\int D\phi' e^{-S[\phi']} e^{\int d^d x(\lambda_0 - \lambda_1)\phi'^4}} \tag{3.12}$$

Although seemingly complicated, the fraction, independent of ϕ, plays the role of a normalization factor. It is practically calculated by simply normalizing the new probability distribution. An observable for λ_1 evaluates as

$$\langle O \rangle_{\lambda_1} = \int D\phi O(\phi) P_{\lambda_0}(\phi) e^{\int d^d x(\lambda_0 - \lambda_1)\phi^4} \frac{\int D\phi' e^{-S[\phi']}}{\int D\phi' e^{-S[\phi']} e^{\int d^d x(\lambda_0 - \lambda_1)\phi'^4}} \tag{3.13}$$

If we had an explicit estimate for $P_{\lambda_0}(\phi)$, this would be possible to evaluate. Getting an estimate would require saving every configuration of ϕ obtained during Monte Carlo sampling. Since ϕ is functional, and therefore very high-dimensional when discretized on a lattice, this would require large amounts of storage space. Therefore, instead of saving the

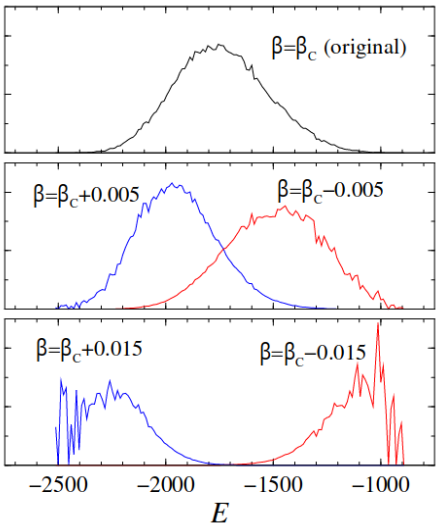

Figure 3.5: A example of a distribution for parameter β_c, reweighted to new β with diminishing quality. Adapted from [53]

whole field ϕ, notice it is sufficient to save the marginal distribution

$$P(K) = \frac{\int D\phi\delta(K - \int d^d x\phi^4)e^{-S[\phi]}}{\int D\phi e^{-S[\phi]}} \tag{3.14}$$

This distribution may be found by Monte Carlo sampling. One can create a histogram over the range of possible $K = \int d^d x\phi^4$, and count the number of configurations

$$N_i = N_{\text{total}} P_i = N_{\text{total}} \int_{b_i} dK \int D\phi P(\phi)\delta(\int d^d x\phi^4 - K) \tag{3.15}$$

that fall into each bin $b_i = [K_i - \Delta K/2, K_i + \Delta K/2]$, $i \in [0, N]$. The smaller the bin size ΔK, the better the estimate, but the more storage is required. To evaluate observables this way requires knowing their marginal dependence on $\int d^d x\phi^4$. This means we also need to know

$$O(K) = \frac{\int D\phi\delta(\int d^d x\phi^4 - K)O(\phi)e^{-S[\phi]}}{\int D\phi\delta(\int d^d x\phi^4 - K)e^{-S[\phi]}} \tag{3.16}$$

In practice, this is done using a second histogram with the same size, summing the observable $O(\phi)$ in the same bin that $\int d^d x\phi_4$ fell into

$$\langle O_i \rangle = \int_{b_i} dK \int D\phi P(\phi)O(\phi)\delta(\int d^d x\phi^4 - K) \tag{3.17}$$

$O_i(\phi) = \int_{b_i} dKO(\phi)\delta(\int d^d x\phi^4 - K)$ and $P_i(\phi) = \int_{b_i} dK\delta(\int d^d x\phi^4 - K)$ are then practically $2N$ additional observables which are calculated during Monte Carlo sampling.
The relation eq. (3.13) is evaluated as

$$\langle O\rangle_{\lambda_1} = \int_\phi O(\phi) P_{\lambda_0}(\phi) e^{\int d^d x(\lambda_0-\lambda_1)\phi^4} \frac{\int D\phi e^{-S[\phi]}}{\int D\phi e^{-S[\phi]} e^{\int d^d x(\lambda_0-\lambda_1)\phi^4}} \tag{3.18}$$

$$\approx \sum_i O_i P_i e^{K_i(\lambda_0-\lambda_1)} \frac{\sum_i P_i}{\sum_i P_i e^{K_i(\lambda_0-\lambda_1)}} \tag{3.19}$$

$$= \frac{\sum_i O_i P_i e^{K_i(\lambda_0-\lambda_1)}}{\sum_i P_i e^{K_i(\lambda_0-\lambda_1)}} \tag{3.20}$$

While in theory, there is no limit to the difference $\lambda_0 - \lambda_1$, in practice, the extrapolation results in an exponential amplification of data points that were sampled with exponentially suppressed probability in the Monte Carlo process. This leads to rapidly growing errors. The macroscopic averages $\int d^d x \phi^n$ also do not vary in the thermodynamic limit $V \to \infty$, such that histogram reweighting becomes less powerful for larger system sizes. In general, the parameter range in which we can extrapolate scales as $\Delta\lambda \propto 1/\sqrt{V}$, and $\Delta\lambda \propto 1/V^\nu$ at phase transitions, with critical exponent ν [53]. Since the phase transition sharpens with the same exponent (see section 2.4.2), histogram reweighting always maintains its usefulness for scanning the critical region.

For complex probabilities, the situation is similar. While the CL probability density $P(\phi_R, \phi_I)$ is not explicitly known, the complex PDF $\rho(\phi) \propto \exp(-S[\phi])$ is. We may treat O_{λ_i} as an observable on ρ by reweighting $e^{S_{\lambda_0} - S_{\lambda_1}}$ into O, i.e.

$$O_{\lambda_1}(\phi) = O(\phi) e^{S_{\lambda_0}[\phi] - S_{\lambda_1}[\phi]} \tag{3.21}$$

This observable is holomorphic, and can be complexified the same way as any other observable. Going back to the explicit example of action eq. (3.10), we can write

$$O_{\lambda_1}(\phi) = O(\phi) e^{\int d^d x \phi^4 (\lambda_0 - \lambda_1)} \tag{3.22}$$

This is once again dependent only on $\int d^d x \phi^4$, now with the complexified $\phi = \phi_R + \phi_I$. In [54] CL trajectories are reweighted. The aim is choosing λ_1 in a regime where CL does not converge correctly, while for λ_0, it gives correct results. The reweighting factor is computed at each configuration and directly absorbed into the averaged observable, discarding the original values at S_{λ_0}.

Here we are instead interested in the continuum of parameters around λ_0, and again use histograms. The only difference is the necessity of knowing both $K = \mathrm{Re} \int d^d x \phi^4$ and $Q = \mathrm{Im} \int d^d x \phi^4$, which results in 2D histograms P_{ij} and O_{ij}, with bins $b_{ij} = [K_i - \Delta K/2, K_i + \Delta K/2] \times [Q_j - \Delta Q/2, Q_j + \Delta Q/2]$. Observables are computed equivalently to eq. (3.20)

$$O = \frac{\sum_{ij} O_{ij} P_{ij} e^{(K_i + iQ_j)(\lambda_0 - \lambda_1)}}{\sum_{ij} P_{ij} e^{(K_i + iQ_j)(\lambda_0 - \lambda_1)}} \tag{3.23}$$

The seemingly complex denominator actually turns out to be real if reweighting a real parameter: P_{ij} in the $N \to \infty$ limit will be exactly equal for positive and negative Q, since the action is symmetric in ϕ_I. Therefore, the imaginary part cancels and we have a proper normalization. In addition to the exponential suppression discussed earlier, complex reweighting now also suffers from a sign problem resulting due to the complex factors in the exponent. Generally, even more caution is necessary when using reweighting for complex actions, but it still proves very helpful at phase transitions. In Figure 4.2, we use it to find the Binder cumulant (eq. (2.135)) around the easy-plane to polar phase transition.

3.3 Entanglement Detection

Due to its intrinsic quantum nature, accessibility of entanglement is diminished the more quantum effects are ignored in approximations. At the same time, it is something becoming increasingly useful with the rise of e.g. entanglement enhanced measurement [55], and is also vital to the theoretical description of some systems. This also makes it an interesting topic to study in field theories. There are Bogoliubov approaches to entanglement where the second order approximation holds [56][57], which are however limited to specific states. Analytic results can be found for conformal field theories, i.e. quantum critical points, where one can find that the entanglement exhibits log scaling, meaning it is not described by local terms [58][59][60]. For classical phase transitions, the quantum correlation length remains finite [60], confirming even BEC type transitions are indeed classical. Quantum Monte Carlo studies have been done for zero temperature quantum field theories [61] and finite temperature quantum lattice models [60]. Here, we present the quantum field theoretic methods commonly used in lattice QFT to quantify entanglement, which are trivial to adapt to complex Langevin with minor inconveniences.

3.3.1 Entanglement Measures

The following entanglement metrics are adapted from [62]. A quantum state is defined as entangled if it cannot be represented as a tensor product of its substates. The state

$$|\psi_1\rangle = \frac{|00\rangle + |01\rangle}{\sqrt{2}} \tag{3.24}$$

can be represented as

$$|\psi_1\rangle = |0\rangle \otimes \frac{(|0\rangle + |1\rangle)}{\sqrt{2}} \tag{3.25}$$

while for the Bell state

$$|\psi_2\rangle = \frac{|01\rangle + |10\rangle}{\sqrt{2}} \tag{3.26}$$

this is not possible. The second state is therefore entangled, while the first isn't. In the same way, a density matrix is considered entangled if it cannot be represented as

$$\rho_{AB} = \rho_A \otimes \rho_B \tag{3.27}$$

with subsystems A and B. A good measure of entanglement for pure states is the entanglement entropy. For a system consisting of subsystems A and B, the reduced density matrix is the partial trace

$$\rho_B = \mathrm{Tr}_A \rho_{AB} \tag{3.28}$$

which is defined as

$$\mathrm{Tr}_A \rho_{AB} = \sum_{\phi_A} \langle \phi_A | \rho_{AB} | \phi_A \rangle \tag{3.29}$$

and ϕ_A being a basis set spanning subsystem A. For a separable state, it holds that

$$\mathrm{Tr}_B(\rho_A \otimes \rho_B) = \rho_A \tag{3.30}$$

This means that if ρ_{AB} is unentangled and pure, then ρ_A must also be pure. For an entangled state, ρ_A is generally mixed. A measure of the purity of a state is the von Neumann entropy, defined as

$$S = -\mathrm{Tr}\rho \log \rho \tag{3.31}$$

which is zero for pure states and nonzero for mixed ones. It can therefore be used as an entanglement measure by calculating

$$S_A = -\mathrm{Tr}\rho_A \log \rho_A \tag{3.32}$$

which is the larger the more entangled a state is. However, entanglement entropy is not a useful measure for mixed states, since it is already finite without entanglement. Instead, one might use the partial transpose. Writing ρ_{AB} as a general combination

$$\rho_{AB} = \sum_{ijkl} p_{ijkl} \left| i \right\rangle \left\langle j \right| \otimes \left| k \right\rangle \left\langle l \right| \tag{3.33}$$

the partial transpose is defined as

$$\rho_{AB}^{T_B} = \sum_{ijkl} p_{ijkl} \left| i \right\rangle \left\langle j \right| \otimes \left| l \right\rangle \left\langle k \right| \tag{3.34}$$

The state is guaranteed to be entangled if $\rho_{AB}^{T_B}$ has a negative eigenvalue. One may define the entanglement negativity

$$N(\rho_{AB}) = \frac{||\rho^{T_B}||_1 - 1}{2} \tag{3.35}$$

as another entanglement measure. Finally, the moments of these measures might be more accessible. For example, the nth Renyi negativity

$$R_n = \frac{\mathrm{Tr}((\rho^{T_B})^n)}{\mathrm{Tr}(\rho^n)} \tag{3.36}$$

can, with some constraints, also serve as an entanglement measure.

3.3.2 Entanglement Measures in Quantum Field Theory

In many body simulations, reconstructing the entire density matrix is infeasible. Therefore, one must find ways to extract entanglement measures from Monte Carlo simulations implicitly. This is usually done through the replica trick, which we briefly described here. Entanglement measurement through the replica trick was first proposed by Calabrese and Cardy [58]. The replica trick for negativity was developed later in a similar manner, we adapt here Wu et al. [60].
The elements of the density matrix ρ of a thermal system are given by

$$\rho(\phi', \phi'') = \langle \phi' | e^{-\beta H} | \phi'' \rangle \tag{3.37}$$

which can be rewritten as a path integral as elaborated in section 2.1.2. We here consider a lattice theory only, although the continuum limit may be taken

$$\rho(\phi', \phi'') = Z^{-1} \int d\phi(x,t) \prod_x \delta(\phi(x,0) - \phi'(x)) \delta(\phi(x,\beta) - \phi''(x)) e^{-S[\phi]} \tag{3.38}$$

Taking the trace $\mathrm{Tr}\rho$ amounts to setting $\psi'(x) = \psi''(x)$ for all x and integrating over their values. This can be seen as *sewing together* these points on the lattice. A partial trace may be taken by sewing together only the endpoints in the region to be traced out.

$$\begin{aligned} \rho_A(\phi', \phi'') = Z^{-1}\mathrm{Tr}_B\rho = \int d\phi(x,t) \prod_{x\in A} \delta(\phi(x,0) - \phi'(x)) \delta(\phi(x,\beta) - \phi''(x)) \\ \times \prod_{x\in B} \delta(\phi(x,0) - \phi(x,\beta)) e^{-S[\phi]} \end{aligned} \tag{3.39}$$

Now, moments $\mathrm{Tr}\rho_A^n$ may be calculated by connecting n copies of ρ_A in imaginary time along the open points in A, and finally taking the trace by setting global periodic boundary conditions between the first and last copy. This is visualized in fig. 3.6. For example, in the case of $n = 2$

$$\mathrm{Tr}\ \rho_A^2 = \sum_{ijk} \langle \phi_A^i | \langle \phi_B^j | e^{-\beta \hat{H}} | \phi_B^j \rangle \langle \phi_B^k | e^{-\beta \hat{H}} | \phi_B^k \rangle | \phi_A^i \rangle \tag{3.40}$$

$$= \sum_{ijkl} \langle \phi_A^i | \langle \phi_B^j | e^{-\beta \hat{H}} | \phi_B^j \rangle | \phi_A^l \rangle \langle \phi_A^l | \langle \phi_B^k | e^{-\beta \hat{H}} | \phi_B^k \rangle | \phi_A^i \rangle \tag{3.41}$$

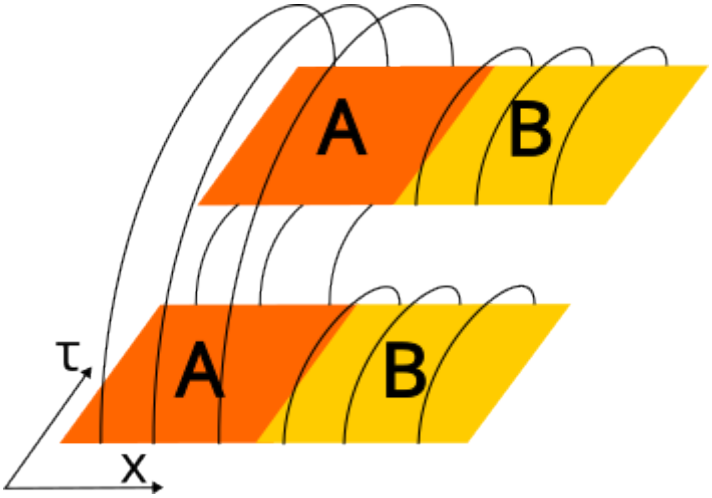

Figure 3.6: The connectivity of Tr ρ_A^2 in imaginary time. Region B is already traced out before taking the square, region A is connected globally

where ϕ_A^i, ϕ_B^i are complete basis sets for the respective regions, such that we can insert them as identity matrices. As a result, taking these moments amounts to changing the topology of the space into one with multiple Riemann sheets.
For entanglement negativity, a different change of topology is necessary. The elements of the transposed density matrix are

$$\rho^{T_B}(\phi'_A, \phi'_B, \phi''_A, \phi''_B) = \langle\phi'_A|\langle\phi'_B|(e^{-\beta H})^{T_B}|\phi''_A\rangle|\phi''_B\rangle \tag{3.42}$$

$$= \langle\phi'_A|\langle\phi''_B|e^{-\beta H}|\phi''_A\rangle|\phi'_B\rangle \tag{3.43}$$

When taking moments of ρ^{T_B}, one has to stitch the segments as $\phi''_{A,k} = \phi'_{A,k+1}$, $\phi''_{B,k} = \phi'_{B,k+1}$ as before. Since for the transposed parts, positions of ϕ' and ϕ'' are swapped, this again results in new topologies, visualized in fig. 3.8. For $n = 1$ and $n = 2$, the topology is trivial (fig. 3.7), so we focus on the $n = 3$ case. Looking only at region B, it reads

$$\text{Tr }(\rho^{T_B})^3 = \sum_{ijk}\langle\phi^i|(e^{-\beta H})^{T_B}|\phi^j\rangle\langle\phi^j|(e^{-\beta H})^{T_B}|\phi^k\rangle\langle\phi^k|(e^{-\beta H})^{T_B}|\phi^i\rangle \tag{3.44}$$

$$= \sum_{ijk}\langle\phi^j|e^{-\beta H}|\phi^i\rangle\langle\phi^k|e^{-\beta H}|\phi^j\rangle\langle\phi^i|e^{-\beta H}|\phi^k\rangle \tag{3.45}$$

While the connectivity is 1-2-3 in region A, it is clearly visible that in region B, the regions connect in order 1-3-2.
With a path integral representation of the reduced and partial transposed density matrix available, we now have to find observables to extract the corresponding entanglement measures. For some Markov chain Monte Carlo methods, one can directly compute partition sum ratios by allowing transitions between topological configurations [63]. For complex Langevin, this is not possible, so we adopt the derivative approach developed by Nakagawa

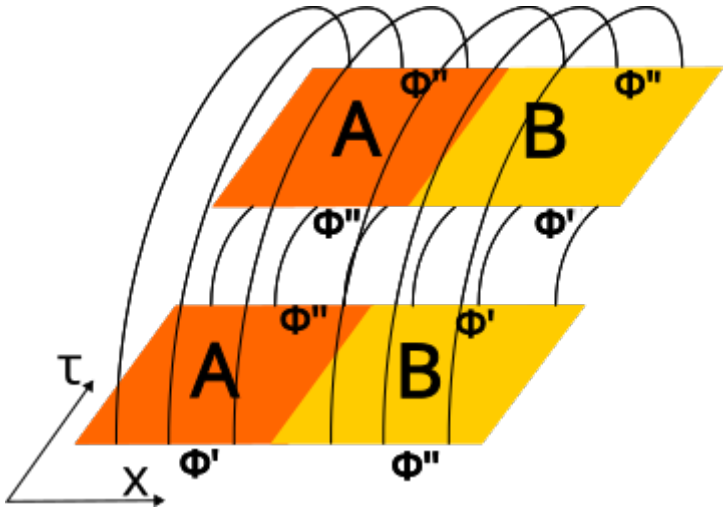

Figure 3.7: The second moment of the partial transposed matrix Tr $(\rho^{T_B})^2$. Its topology is unchanged from Tr $(\rho)^2$ and can therefore not contain any new information about entanglement.

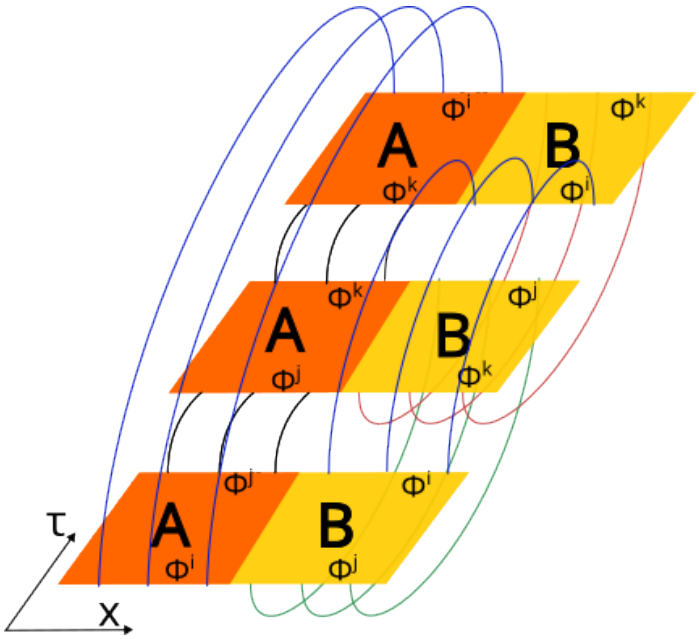

Figure 3.8: The third moment of the partial transposed matrix Tr $(\rho^{T_B})^3$ has a nontrivial topology.

et al. [61].
To measure entanglement entropy directly, we have to lower the temperature close enough to zero to find an almost pure state, which requires a large temporal extent of the lattice. The entanglement entropy can be written as the limit

$$S_A = -\mathrm{Tr}\rho_A \log \rho_A = -\lim_{n\to 1} \frac{\partial}{\partial n} \log \mathrm{Tr}\rho_A^n = -\lim_{n\to 1} \frac{\partial}{\partial n} \log\left(\frac{Z(l,n)}{Z^n}\right) \tag{3.46}$$

with $Z(l,n)$ being the partition function with the topology described in eq. (3.41) imposed, with B having spatial extent l. Even without the limit, this expression describes the nth Renyi entropy [58], a quantity sometimes useful and more accessible than the standard entropy. We make use of Renyi generalizations for the negativity, since taking the $n \to 1$ limit is not possible for a matrix one norm the same way it is for the entropy.
The entropy itself is generally UV divergent, so we focus on the derivative

$$\frac{\partial S_A}{\partial l} = -\lim_{n\to 1} \frac{\partial}{\partial n}\frac{\partial}{\partial l} \log Z(l,n) = -\lim_{n\to 1} \frac{\partial}{\partial n}\frac{\partial}{\partial l} F(l,n) \tag{3.47}$$

with free energy $F(l,n) = \log Z(l,n)$. We now approximate the derivative in n to be discrete

$$\frac{\partial S_A}{\partial l} \approx -\lim_{n\to 1} \frac{\partial}{\partial l}[F(l,n+1) - F(l,n)] \tag{3.48}$$

The free energy with $n = 1$ is just the partition function with standard topology, which is independent of l, so its derivative is zero. We can then also discretize the l derivative of the remaining term

$$\frac{\partial S_A}{\partial l} \approx -\frac{F(l+a,2) - F(l,2)}{a}. \tag{3.49}$$

To calculate this ratio, we can define an interpolating action, which works similar to a generating functional. The action reads

$$S_\alpha = (1-\alpha)S_l[\phi] + \alpha S_{l+a}[\phi]. \tag{3.50}$$

With S_l representing the action with extent of A equal to l. The difference in eq. (3.49) can now be written as

$$F(l+a,2) - F(l,2) = \int_0^1 d\alpha \frac{\partial}{\partial \alpha} \log Z(l,\alpha) = \int_0^1 d\alpha \langle S_{l+a}[\phi] - S_l[\phi]\rangle_{S_\alpha}. \tag{3.51}$$

After the integral is discretized, this is a sum of expectation values we can evaluate using the Langevin process.
This is a very expensive calculation. Multiple simulations are required to evaluate the integral for one value of l. There are multiple sign problems: For a complex action, the action expectation value has an imaginary part that is canceled out, and in the integral, there is a cancellation between positive and negative parts (see fig. 4.7 for an applied example).

This makes the integral quite hard to calculate, but using kernel acceleration it remains in the range of possibilities for medium size lattices.
For the negativity, we perform the same trick, except looking at

$$\frac{\partial R_3}{\partial l} = -\frac{\partial}{\partial l} \log(Z_T(l)) \tag{3.52}$$

where Z_T is the partition function with an area A of size l transposed. Since no limit in n is taken, this calculation should generally be more accurate. We can directly discretize in the same way

$$\frac{\partial R_3}{\partial l} = -\frac{F_T(l+a) - F_T(l)}{a} \tag{3.53}$$

and calculate this difference with a crossover action completely analogous to eq. (3.50). As said before, the negativity has the advantage of being meaningful for nonzero temperatures where less analytical calculations are possible, which is why it is the main object of our studies.

Chapter 4

Application of Complex Langevin to the Spin-1 Bose Gas

The application of complex Langevin to the fied of ultracold gases is still in its infancy. Until now, simulation of single component BECs in 3D [37], the BKT transition [64] and dipolar gases has been possible. Here we analyze a multicomponent system, the spin-1 gas. We present the results of our multiple studies. The explicit parameters used are given in 6.1

4.1 Complex Langevin Simulation of a Spin-1 Gas

The Hamiltonian of a spin-1 gas, as derived in section 2.3, is given by

$$H = \frac{1}{2M}\nabla\psi_m^\dagger\nabla\psi_m + \mu\psi_m^\dagger\psi_m + qm^2\psi_m^\dagger\psi_m + \frac{c_0}{2}\psi_a^\dagger\psi_b^\dagger\psi_b\psi_a + \frac{c_1}{2}\psi_{a'}^\dagger\psi_a^\dagger\sigma_{ab}^\nu\sigma_{a'b'}^\nu\psi_b\psi_{b'}. \quad (4.1)$$

This can be transformed into an action using the coherent state path integral formalism, resulting in

$$S = \oint_0^\beta d\tau(-\psi\partial_\tau\bar{\psi} + H(\psi,\bar{\psi})) \quad (4.2)$$

which as discussed results in a sign problem due to the first order time derivative. We aim to use complex Langevin simulations to overcome this sign problem, and show quantum corrections to the mean field and Bogoliubov approximations.

$m=-1$				$m=0$				$m=1$			
l_{abc}	a	b	c	l_{abc}	a	b	c	l_{abc}	a	b	c
1	0	0	0	1	0	0	1	-1	0	0	2
1	1	0	1	2	1	0	2	1	0	1	1
-1	2	0	2	1	2	1	2	1	1	1	2
1	2	1	1					1	2	2	2

Table 4.1: The multiplicators for each component m of the spin derivative, used in eq. (4.3)

4.2 Implementation

The Langevin equations are given by

$$\frac{\partial \phi^i_{\tau,x}}{\partial \theta} = -\frac{\partial S[\phi,\bar{\phi}]}{\partial \bar{\phi}^i_{\tau,x}} + \eta = \eta + a_s^3 \Bigg\{ (\phi^i_{\tau-1,x} - \phi^i_{\tau,x}) + a_\tau \left(1/2 M \Delta \phi^i_{\tau-1,x} + (\mu - q m^2)\phi^i_{\tau-1,x} - c_0 \phi^i_{\tau-1,x} \sum_j \bar{\phi}^j_{\tau,x} \phi^j_{\tau-1,x} + c_1 \sum_{abc \in K_i} l_{abc} \bar{\phi}^a_{\tau,x} \phi^b_{\tau-1,x} \phi^c_{\tau-1,x} \right) \Bigg\} \tag{4.3}$$

$$\frac{\partial \bar{\phi}^i_{\tau,x}}{\partial \theta} = -\frac{\partial S[\phi,\bar{\phi}]}{\partial \phi^i_{\tau,x}} + \eta^* = \eta^* + a_s^3 \Bigg\{ (\bar{\phi}^i_{\tau+1,x} - \bar{\phi}^i_{\tau,x}) + a_\tau \left(1/2 M \Delta \bar{\phi}^i_{\tau+1,x} + (\mu - q m^2)\bar{\phi}^i_{\tau+1,x} - c_0 \bar{\phi}^i_{\tau+1,x} \sum_j \bar{\phi}^j_{\tau+1,x} \phi^j_{\tau,x} + c_1 \sum_{abc \in K_i} l_{abc} \phi^a_{\tau,x} \bar{\phi}^b_{\tau+1,x} \bar{\phi}^c_{\tau+1,x} \right) \Bigg\}. \tag{4.4}$$

Calculating the derivative of the spin-spin interaction term using Pauli matrix multiplication and lookup involves a lot of multiplication by zero and therefore wastes runtime. We instead precalculate the multipliers l_{abc} and nonzero index combinations abc for each index i in the set K_i. They are explicitly given in table 4.1. The different indices in imaginary time result from the particular discretization of the CSPI, see eq. (2.25). Simulations are done in lattice units. Apart from setting $\hbar = 1$, $k_B = 1$, which we have already assumed before, we also set $2M = a_s^{-1} = 1$. This way, all other constants are implicitly given in units of the lattice spacing a_s.

For the Laplacian Δ, there are multiple implementations. The simplest discretization is given by an $O(a^2)$ lattice second derivative, i.e. in 1D

$$\Delta A_{i,n} = A_{i,n+1} - 2A_{i,n} + A_{i,n-1}. \tag{4.5}$$

However, the corresponding momenta in Fourier space are given by a crystal-like dispersion [37]

$$k_i^2 = \frac{4}{a_s^2} \sin^2\left(\frac{\pi j_i}{N_s}\right), \tag{4.6}$$

with momentum lattice points j_i in dimension i. Instead, we opt for a spectral implementation [64]

$$\Delta A_n = -\frac{1}{N_s}\sum_{mn'=0}^{N_s-1} \exp\left(i\frac{2\pi}{N_s}m(n-n')\right)\left|\frac{2\pi m}{N_s a_s}\right|^2 A_{n'}. \tag{4.7}$$

This form seems to involve $O(N_s^2)$ multiplications (with amount of lattice sites N_s), in contrast to the $O(N_s)$ multiplications in the simple discretization. However, implemented using using the Fast Fourier Transform (FFT), it only has $O(N \log N)$ complexity. It is then simply $\Delta A_{i,n} \sim FFT^{-1}(-k^2 \times FFT(A_{i,n}))$. This makes this implementation viable, since its resulting spectrum is identical to the continuum spectrum.

$$k_i^2 = \frac{4\pi^2}{a_s^2}\frac{j_i^2}{N_s^2}. \tag{4.8}$$

The update of the free part of the action can be calculated analytically in momentum space [65]

$$\frac{\partial S_{\text{free}}}{\partial \phi} = [1-(1-a_\tau\frac{k^2}{2M}+a_\tau\mu)e^{-2\pi ij/N_\tau}]\phi \tag{4.9}$$

with imaginary time step a_τ, and Matsubara frequencies $\omega_j = 2\pi j/\beta$. For $\frac{\partial\phi}{\partial\theta} = -\frac{\partial S}{\partial\phi}$ to be stable, it has to hold

$$0 < a_\tau(\frac{k_{max}^2}{2M}-\mu) < 2. \tag{4.10}$$

This gives a maximum imaginary time step

$$a_\tau < \frac{2}{\frac{k^2}{2M}-\mu}. \tag{4.11}$$

Since we are in a symmetry broken phase, we approximate $\mu = 0$. The maximum kinetic energy on a d-dimensional lattice, with spectral Laplacian and in lattice units $a_s = 1$, $2M = 1$, is $k_{max}^2 = d\pi^2$. The maximum time step in three dimensions is then

$$a_\tau^{\max} = \frac{2}{3\pi^2} \approx 0.0675. \tag{4.12}$$

This puts a practical limit on the imaginary time step size, and therefore the maximum extent of the imaginary time direction and the lowest temperatures that can be reached for a given lattice size. There might be a possibility to construct the CSPI in a way where this limit doesn't exist [6], but to our knowledge this formulation has not been investigated for quantum fields. Since the discretization error scales linearly in time due to the first order derivative, it is anyways advisable to keep the time step as low as possible.

Atom	a_0 [a.u.]	a_2 [a.u.]
^{23}Na	52.98 ± 0.4	47.36 ± 0.8
^{87}Rb	100.4 ± 0.1	101.8 ± 0.2

Table 4.2: Scattering lengths of sodium-23 and rubidium-87. They lie closely together, leading to a separation $|c_0| \approx 10^2 |c_1|$

4.3 Length Scales

QFT on a lattice explicitly implements two scales: The lattice spacing a_s, and the lattice size $L = N_s a_s$. In Bose-Einstein condensates, there are multiple intrinsic physical length scales which are relevant to the behavior of the system. The s-wave scattering length a, described in section 2.3.1, quantifies the interaction strength between the particles. To assume a contact interaction, we have to leave $a << a_s$. Otherwise, the microscopic structure of the interaction potential would have to be taken into account.
The healing length $\xi = \frac{1}{\sqrt{2Mnc}}$ specifies the distance in which the condensate phase *heals* from defects and becomes coherent. In the spin-1 condensate, we observe two different healing lengths: One for global phase coherence, $\xi_d = \frac{1}{\sqrt{2Mnc_0}}$, and one for coherence of the transverse polarization, $\xi_s = \frac{1}{\sqrt{2Mnc_1}}$. Both ξ_d and ξ_s should be above the lattice spacing a_s, but well below the system size L to avoid finite-size effects. Lastly, the thermal wavelength $\lambda_T = \sqrt{\frac{2\pi}{MT}}$ should be above a_s and below L if one wants to observe finite temperature effects, but can be larger than L if more interested in the zero temperature limit.

4.4 Choice of Parameters

Our standard set of parameters is $\mu = 0.25 a_s^{-1}$, $c_0 = 0.05 a_s^2$, $c_1 = 0.02 a_s^2$. This is a toy set of parameters and does not directly correspond to any real gas, see table 4.2. For values in the range of rubidium's, the ferromagnetic choice, the small value of $|c_1| \approx 10^{-2} |c_0|$ results in numerical problems: The evolution in the spin changing collisions is very slow in comparison to the density. Additionally, the resulting spin healing length is a factor 10 larger than the density healing length, resulting in increased finite-size effects. This makes good simulations of rubidium in 3D difficult. Simulations in 1D or 2D might be more feasible, but are out of scope for this thesis. The chosen parameters, however, lie in the typical diluteness range $\eta \approx 10^{-3} - 10^{-4}$ of an experimentally realized rubidium BEC. The diluteness also places a limit on the accessible parameter regime, with CL becoming unstable at around $\eta \geq 10^{-2}$. Another choice of atom would be potassium, whose interactions are weak but highly tunable using Feshbach resonances, which is a topic of current experimental research.

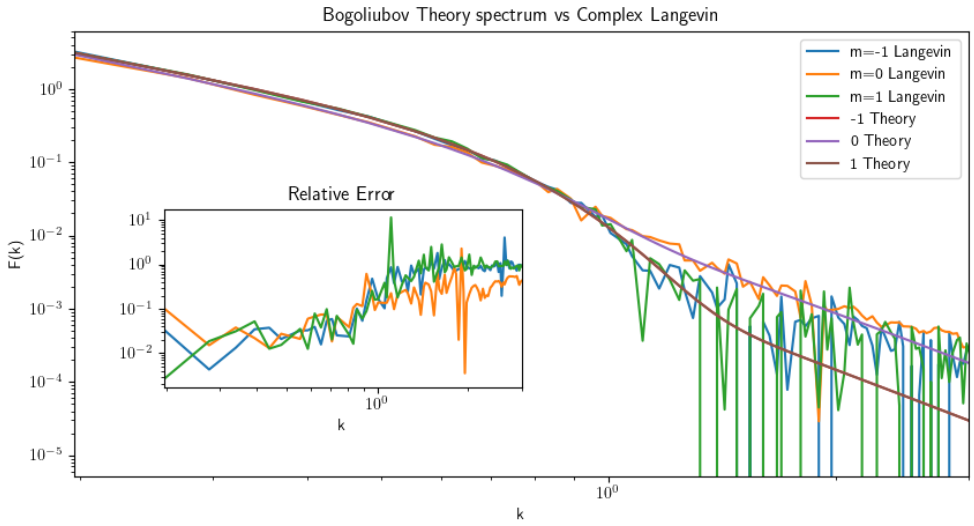

Figure 4.1: The Bogoliubov occupation numbers determined from theory and from CL simulation. They are well recovered for low momenta, while statistical noise strongly shows for high momenta that are occupied to a low level and mainly due to quantum fluctuations. Still, we converge to the correct solution for long enough runs.

4.5 Confirmation of Bogoliubov Theory

Bogoliubov theory makes explicit predictions about the average occupation numbers of different momentum modes k. It is usually very accurate while away from phase transitions and at sufficiently low temperatures. We can calculate the occupation of momentum modes in CL simulations by Fourier transforming the field $\phi_i^k(k) = \int e^{-ikx}\phi_i(x)$, $\bar{\phi}_i^k = \int e^{ikx}\bar{\phi}_i(x)$ (this is an FFT in implementation) and calculating

$$F(p) = \sum_{p=|p|} \bar{\phi}_k(p)\phi_k(p) \tag{4.13}$$

summing over modes with equal momentum, on the same spherical surface. The results are shown in fig. 4.1. The agreement is very good at low momenta, but decreases at high momenta mainly due to numerical noise. The noise appears due to the multiple orders of magnitude of occupation numbers covered by the spectrum. It is less severe for higher temperature occupations, which we mainly consider here.

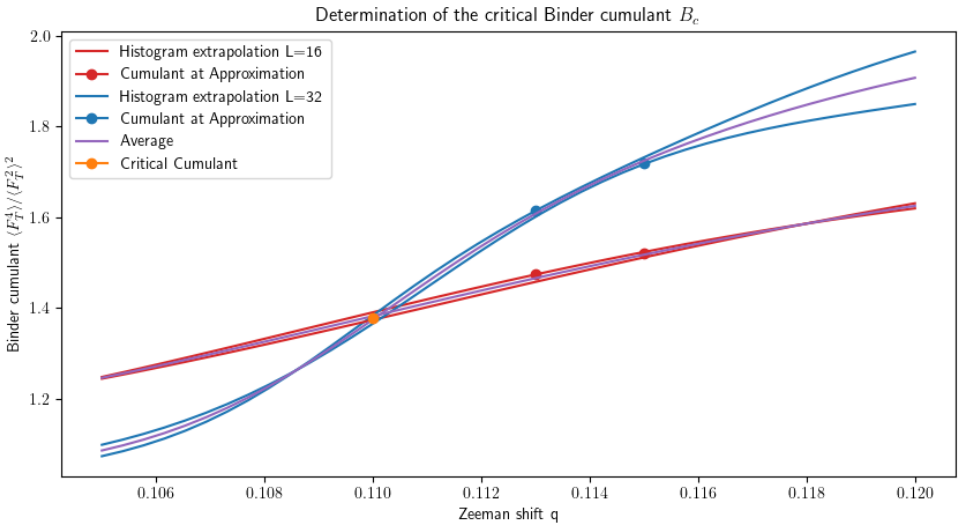

Figure 4.2: Determination of the Binder cumulant from histogram reweighting. We find $B_c = 1.378 \pm 0.019$. The error is estimated from the distance of the extrapolations from each other.

4.6 Determination of the critical Binder cumulant

We perform two complex Langevin Simulations close to the EP-Polar finite temperature phase transition for two different lattice sizes. We extrapolate the results using histogram reweighting, and determine the critical Binder cumulant as the crossing of the average extrapolations (see fig. 4.2). We find

$$B_c = 1.378 \pm 0.019, \tag{4.14}$$

with error estimated from difference of extrapolations. This is not in agreement with the known 3D $O(2)$ model Binder cumulant from [46]

$$B_c = 1.2430 \pm 0.0005 \tag{4.15}$$

More accurate investigations are required to determine if this is due to a different universality class, numerical bias, or additional effects. For now, we work with the Binder cumulant determined here.

4.7 Finite Temperature Phase Diagram

The effects of finite temperature on the phase diagram of the spin-1 gas have been studied in various ways [40][66]. Until now, no exact quantum simulation has been done to determine it. However, there exist very accurate approximations. Away from the QCP, the self consistent second-order approximation, developed in [40], should be quite accurate. We briefly present it here and use it as a comparison to our studies, with a full description including the explicit approximations found in [40].
We make a background field ansatz, writing

$$\hat{\psi}(r) = \phi + \hat{\delta}(r) \tag{4.16}$$

Inserting this into the Hamiltonian, we end up with higher order terms in δ. These terms are reduced to second order by making a mean field approximation

$$\begin{gathered}\delta_l^\dagger \hat{\delta}_j \delta_k \simeq \tilde{n}_{ij}\delta_k + \tilde{n}_{ik}\hat{\delta}_j + \hat{\delta}_l^\dagger \tilde{m}_{jk}, \\ \hat{\delta}_j^\dagger \delta_j^\dagger \delta_k \delta_l \simeq \tilde{n}_{ik}\hat{\delta}_j^\dagger \hat{\delta}_l + \tilde{n}_{jl}\hat{\delta}_j^\dagger \hat{\delta}_k - \tilde{n}_{ik}\tilde{n}_{jl} + \tilde{n}_{il}\hat{\delta}_j^\dagger \hat{\delta}_k \\ +\tilde{n}_{jk}\delta_l^\dagger \delta_l - \tilde{n}_{il}\tilde{n}_{jk} + \tilde{m}_{ij}^* \delta_k \hat{\delta}_l \\ +\tilde{m}_{kl}\delta_l^\dagger \delta_j^\dagger - \tilde{m}_{ij}^* \tilde{m}_{kl},\end{gathered} \tag{4.17}$$

with classical non-condensate density $\tilde{n}_{ij} = \langle \delta_i^\dagger \delta_j \rangle$ and anomalous density $\tilde{m}_{ij} = \langle \delta_i \delta_j \rangle$. In classical Bogoliubov theory, we set $\tilde{n}_{ij} = \tilde{m}_{ij} = 0$. Here, instead we solve the model self-consistently in a numerical way, making it accurate up to higher temperatures, where a large part of the condensate is depleted. We start with $\tilde{n}_{ij} = 0$. First, we perform gradient descent in ϕ to minimize the Hamiltonian

$$\frac{\partial H}{\partial \phi} = 0 \tag{4.18}$$

such that terms linear in δ vanish. We then perform a Bogoliubov calculation, rewriting the terms containing δ as

$$\hat{H}^{(2)} = \sum_k \sum_{ij} \left[\delta_i^\dagger A_{ij}^k \delta_j + \frac{1}{2}\left(\delta_j^\dagger B_{ij}^k \delta_j^\dagger + \delta_i (B_{ij}^k)^* \delta_j \right) \right], \tag{4.19}$$

and finding the eigenvectors and eigenvalues to the Bogoliubov-de Gennes equation for each momentum k

$$\begin{pmatrix} A_{ij}^k & B_{ij}^k \\ -B_{ij}^{k*} & -A_{ij}^{k*} \end{pmatrix} \begin{pmatrix} u_j^{(k,\alpha)} \\ v_j^{(k,\alpha)} \end{pmatrix} = \epsilon^{(k,\alpha)} \begin{pmatrix} u_i^{(k,\alpha)} \\ v_i^{(k,\alpha)} \end{pmatrix} \tag{4.20}$$

with mode number α. Performing these steps once recovers the spectrum found analytically in section 2.3.6. We can now calculate the depletion

$$\begin{aligned}\tilde{n}_{ij} = &\sum_{k,\alpha} \Big\{ u_i^{(k,\alpha)*} u_j^{(k,\alpha)} f\left(\epsilon^{(k,\alpha)}\right) \\ &+ v_i^{(k,\alpha)} v_j^{(k,\alpha)*} \left[f\left(\epsilon^{(k,\alpha)}\right) + 1 \right] \Big\}.\end{aligned} \tag{4.21}$$

This can now be reinserted into the Hamiltonian, and the steps (eq. (4.18) - eq. (4.21)) are iterated with the new $\tilde{n}_{ij}$ until convergence. In this approximation, only the anomalous average $\tilde{m}_{ij}$ is set to zero, corresponding to no phase coherence in the thermal cloud. Higher order interactions are not neglected, but considered as quadratic interactions with the thermal cloud. We choose the momentum modes k to be the same as those on the lattice used for complex Langevin simulations. In contrast to [40], we do enforce the particle number N to be constant, since we are comparing to simulations in the grand canonical ensemble.

We are interested in the thermal transition from the polar to the easy-plane phase, which

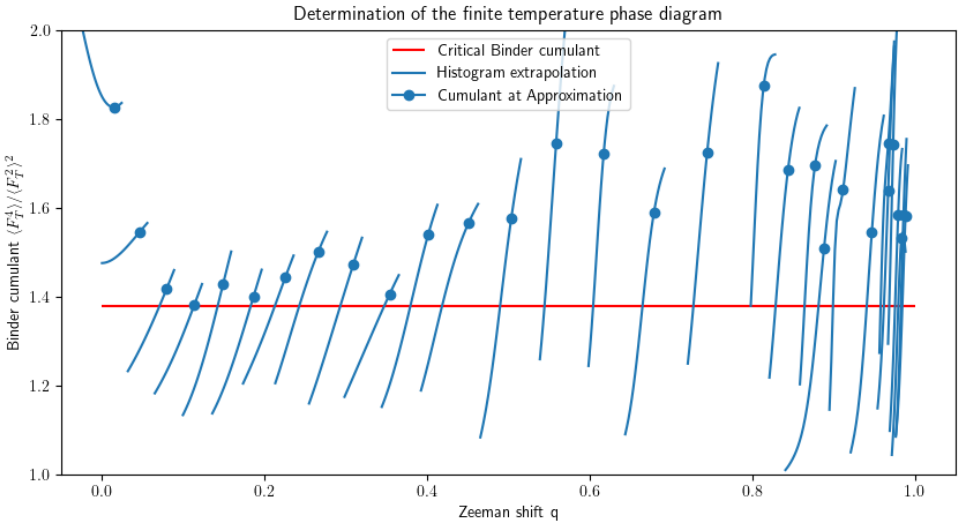

Figure 4.3: The procedure of finding the corrected critical point. The Binder cumulant at the approximated critical coupling (marked by a dot) is extrapolated across the phase transition using histogram reweighting. The phase transition is located where the cumulant takes its critical value. Values close to $q = 0$ are influenced by the phase transition to the ferromagnetic phase and ignored for later analysis. Values close to the critical coupling are sampled more densely due to the rapidly decreasing critical temperature.

is at low temperatures also controlled by a quantum critical point. To find the critical line $T_c(q)$ in the self consistent approximation, we determine the phase of the system using the order parameter $F_T = \sqrt{F_x^2 + F_y^2}$, the transverse polarization. It is only nonzero in the symmetry-broken EP phase. We then use a bisection algorithm [67] to find the critical temperature to arbitrary accuracy for any given coupling q. Since Langevin simulations

are a lot more computationally expensive, we use the approximation as an ansatz, and run CL simulations at the critical parameters found by it. It is important to perform the Bogoliubov calculation using the renormalized parameters. Using histogram reweighting, we extrapolate the Binder cumulant across the phase transition and determine the critical value q_c (see fig. 4.3). This way, only one Langevin simulation is needed per temperature, greatly reducing the amount of compute time needed. We find that the critical coupling is reduced in the medium temperature regime, while receiving little correction for high and low temperatures (fig. 4.4). This might be due to the thermal cloud being magnetized oppositely to the condensate due to higher order interactions. Further investigations could be performed measuring condensate and non-condensate polarization separately to confirm this.

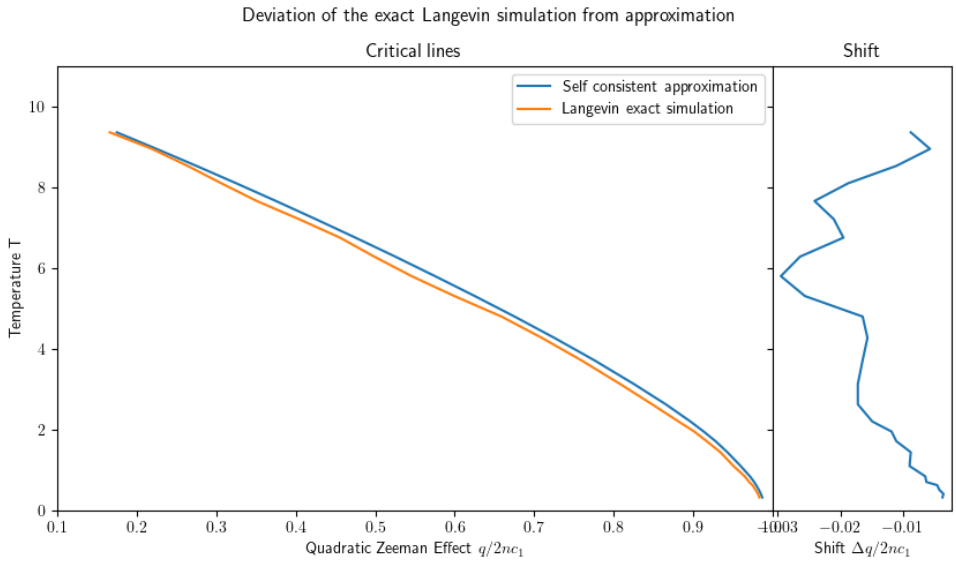

Figure 4.4: The finite temperature critical line from self consistent approximation and CL simulation. Running averaging is applied to both curves to filter out statistical noise. We find that the shift becomes maximal around $q = nc_1$.

4.8 Shift of the Critical Coupling

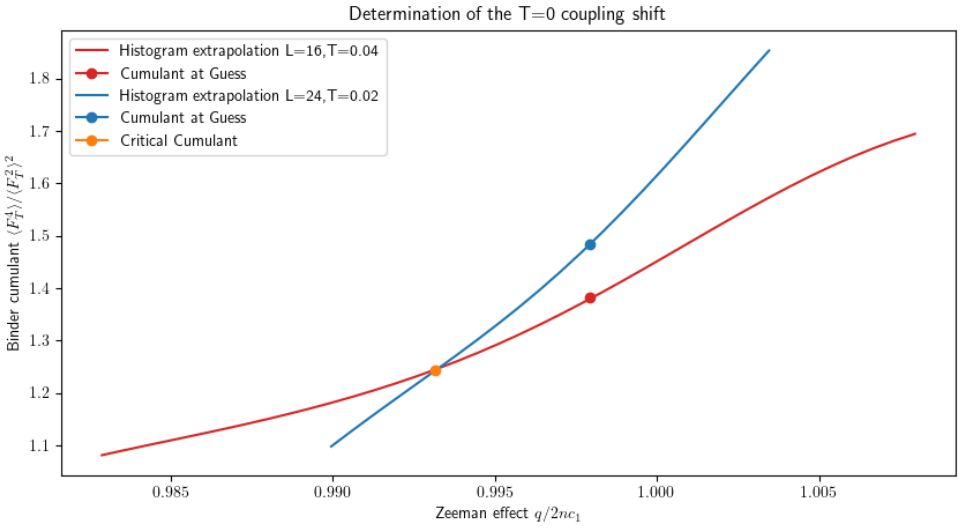

Figure 4.5: Determination of the critical coupling shift from mean field theory ($q_c = 1$). We find a shift of the critical coupling of less than one percent in direction of the EP phase. This is in contrast to the strong shift in the opposite direction found in [66] with different parameters. Further investigation is required to find the behavior of the quantum corrections to the critical coupling for any parameters.

In [66], at $T = 0$, a shift of the critical coupling into the polar phase is found. Extrapolating to $T = 0$ in CL simulations involves increasing a four-dimensional volume. Together with the limit on the imaginary time step eq. (4.11), this sets computational limits on the quality of the extrapolation. Kawaguchi, Phuc, and Blakie [66] also predict a qualitative difference of the thermal clouds effect on the condensate around $T = T_c/100$, making an extrapolation from higher temperatures impossible[1]. To make a reasonable approximation, we simulate on a small spatial lattice with a large temporal extent and determine the critical coupling through the critical Binder cumulant. It is different from the finite temperature cumulant since the universality class generally changes [44], and we increase both spatial and imaginary time dimension for correct comparison. We find

$$B_c = 1.24 \text{ (no error determined)} \tag{4.22}$$

and deviation from the mean field coupling

$$\frac{q_{c,MF} - q_{c,CL}}{q_{c,MF}} = 6.8 \times 10^{-3} \text{ (no error determined)} \tag{4.23}$$

[1] We do not find this shift with the parameters chosen in this thesis.

We did not track exact error values but may infer an error of around 10% from the amount of statistics generated. The Binder cumulant agrees with the literature value of the $O(2)$ Binder cumulant (eq. (4.15)), suggesting the quantum phase transition is indeed part of a different universality class. Since the Binder cumulant for small lattices includes non-universal corrections in general, we do not interpret our result as quantitatively accurate. We do however not find a strong, multiple percent shift of the coupling into the polar phase, as Phuc, Kawaguchi, and Ueda [40] find with a different set of parameters. Other quantum Monte Carlo methods that specifically find the zero temperature ground state might be better equipped for determination of zero temperature properties [15].

4.9 Entanglement Negativity Scaling with Lattice Size

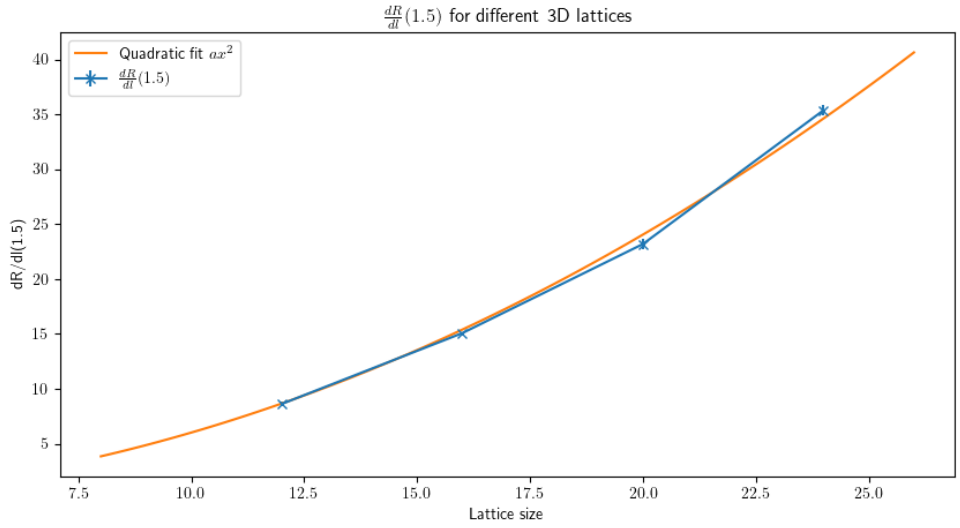

Figure 4.6: The derivative of the third Renyi negativity depending on lattice size. We find a quadratic scaling, confirming theory.

In theory, entanglement between two regions is proportional to the area separating the regions [58]. For our straight cut through a 3D lattice, this results in a scaling with L^2. In fig. 4.6, we show the differential of the third Renyi negativity depending on lattice size. We find it fits a quadratic function reasonably well, confirming that Renyi negativity quantifies entanglement.

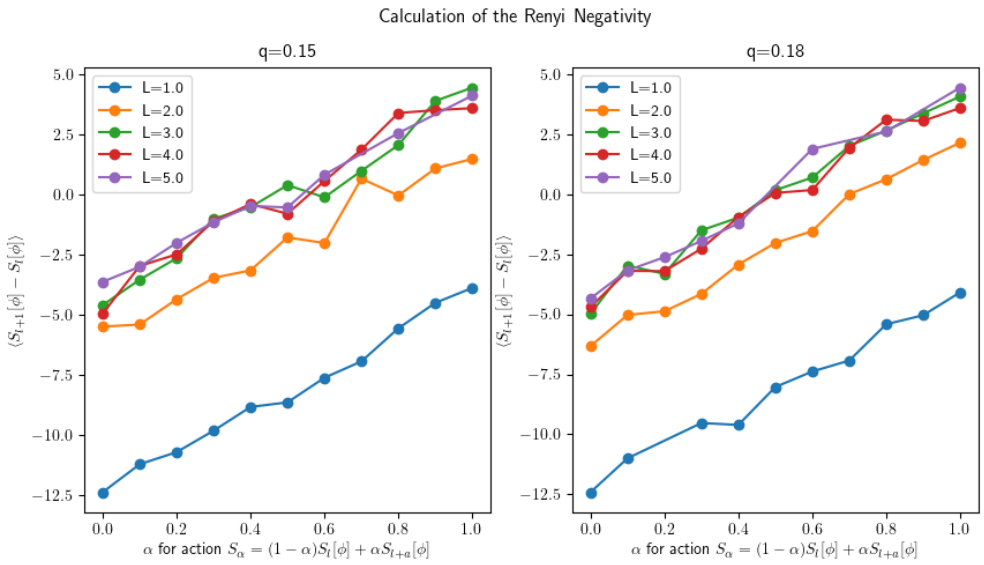

Figure 4.7: The calculation of the Renyi Negativity. We plot the difference in action for each crossover action S_α. The negativity derivative is then given by the integral over all points. Each point amounts to a 24 h simulation, making this calculation very expensive.

4.10 Entanglement Negativity at the Classical Phase Transition

We perform a finite temperature simulation for a quantum field theory with a sign problem, which to our knowledge is the first time entanglement measures have been obtained from a complex Langevin simulation. This is especially interesting since there are connections between Berry phases and entanglement [68], which might in the future be investigated further using CL. We find no increased range of Renyi negativity at the polar to easy plane condensation away from the critical point (fig. 4.8), suggesting the phase transition is still completely classical without imaginary time scaling. Further studies should be conducted for lower temperature systems in the critical scaling regime.

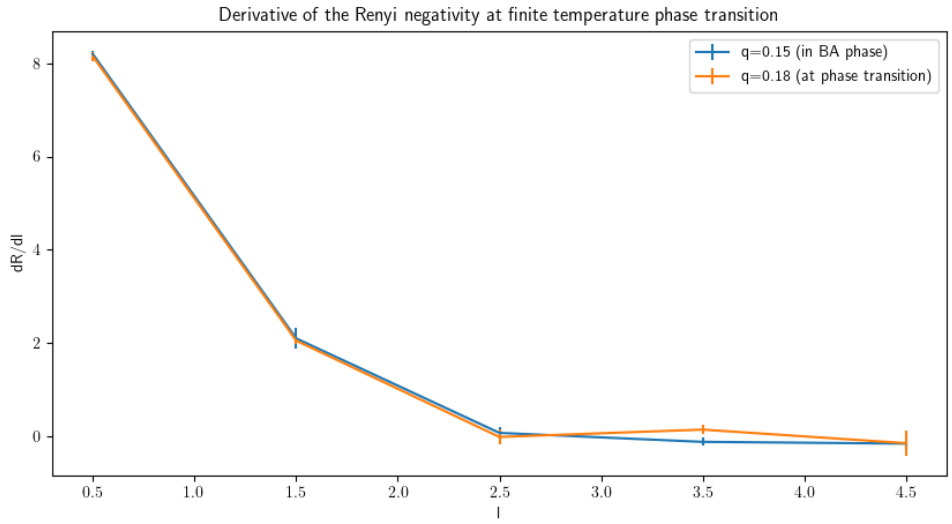

Figure 4.8: The derivative of the third Renyi negativity $\frac{\partial R_3}{\partial l}$ at the classical phase transition ($q = 0.18$) vs away from the phase transition ($q = 0.15$), error bars are estimated by removing values from the numerical integrals. The negativity is larger for lower l, showing local entanglement as expected. No significant difference can be seen between the different parameters.

Chapter 5

Conclusion and Outlook

In the growing field of ultracold Bose gases, CL provides a unique exact way of calculating equilibrium properties numerically. While CL is routinely applied in the field of lattice QCD with large success, its application is still in its infancy for the field of Bose gases. A full quantum field theoretical simulation of Bose gases is not just interesting as another approach to test their general properties, but also beneficial to further the study of quantum field theories using BECs as a testing ground. In this thesis, we have shown the viability of complex Langevin being applied to a gas with a complex interaction structure: the spinor Bose gas. We found a significant deviation of the critical line from the best available approximation even at finite temperatures, which could be detectable in experiments. Confirming our results for entanglement experimentally might be possible, but is considerably more complex.

We have also adapted multiple methods from standard lattice QFT to complex Langevin simulations. The complexification only requires small adjustments to the methods. Kernel acceleration has been used for Langevin simulation of QFTs without a sign problem in the past [51]. It is also a staple in Hamiltonian Monte Carlo algorithms today, where the kernel is known as a mass matrix [14]. Kernels themselves are used for stabilization of diverging complex Langevin trajectories [9], but not for acceleration. We bring complex Langevin up to the level of standard Monte Carlo methods, by using kernels for accelerating the Langevin dynamics. This technique should be adaptable to lattice gauge theories, and might be used to explore the phase diagram of high-density QCD in the future.

Histogram reweighting is easily adaptable to CL. We show that it is effective at extrapolating parameters, even when confronted with a sign problem from complexified fields. This makes scanning large parts of a parameter space much more feasible.

The possibility of entanglement calculation for ultracold Bose systems is an exciting prospect, since it allows finding highly entangled equilibrium states even at finite temperature. These highly entangled states might be practically useful [69], and complex Langevin analysis could provide more insight into their physics. Our current results do not show an entanglement increase at the finite-temperature phase transition, so further studies are required to

find if there is any entanglement increase in the spin-1 gas.
In the future, complex Langevin can hopefully be applied to more systems in the realm of ultracold gases. 1D-gases in a finite volume exhibit special coherence properties and phase diagrams, with a larger influence from quantum effects than their 3D counterparts. With the 1D Lieb-Liniger model being integrable [70], 1D systems would also be useful for complex Langevin to test against. Other interaction structures might also be analyzed, like spin-2 gases [35] and particle mixtures of both bosons and fermions. More, setups like black hole analogues [71] in BECs might be accessible. Successfully entending the validity of complex Langevin into the high density, non-perturbative regime, where it could be used to describe superfluid helium [72], would be a great advancement. While complex Langevin seems to be highly divergent for real-time fields [73], it might be possible to simulate strongly dissipative systems for short real-time scales. These real-time simulations could be used, for example, for the computation of vortex dynamics.
Methodically, there are some advances in the Hamiltonian/Hybrid Monte Carlo community not yet common in complex Langevin simulations. Apart from kernel acceleration, which we introduced in this thesis, the underdamped Langevin equation [74], an equivalent formulation to the overdamped Langevin equation in thesis, is commonly used in HMC and uses an additional momentum variable for its dynamics[14]. Using the underdamped Langevin equation can be compared to using momentum for gradient descent in machine learning, and also allows for pseudo-symplectic integrators. This might provide more stability and accelerated dynamics for certain systems. Other techniques used in HMC, even if not directly applicable in CL due to the missing Metropolis step, might prove adaptable for the stochastic dynamics of complex Langevin.
We see complex Langevin as a way of overcoming the sign problem which still has a lot of room for exploration, and might provide great insights into new systems in the future.

Chapter 6

Appendix

6.1 Appendix A: Implementation and Parameter Details of the Simulation

All Langevin simulations are done using the cupy [75] package for GPU accelerated computing. Calculations are done on the bwUniCluster 2.0 high performance cluster, and each job is run on a single NVIDIA V100, A100 or H100 GPU. All jobs for final results run for 24 hours wall time, and all lattice sizes are $32 \times 32 \times 32$, unless mentioned otherwise.

Figure	$\mu[a_s^-1]$	$c_0[a_s^2]$	$c_1[a_s^2]$	T $[a_s^-1]$	$d\theta$	μ_{eff}
3.2, 3.3	0.001	0.1	0.00	0.625	3×10^{-4}	1/32
2.6	0.25	0.05	0.02	0.5	-	-
4.1	0.25	0.05	0.02	0.5	3×10^{-4}	0.25
4.3,4.4,4.2	0.25	0.05	0.02	varies	3×10^{-4}	0.25
4.5	0.25	0.05	0.02	in Fig	3×10^{-4}	0.25
4.6	0.25	0.05	0.02	0.625	3×10^{-4}	0.25
4.7, 4.8	0.25	0.5	0.2	0.625	3×10^{-3}	0.25[1]

Table 6.1: The parameters for the different simulations, sorted by the figures in which they appear. Note that these are the bare parameters supplied to the CL simulation

6.2 Appendix B: Code

Code will be made available at `https://github.com/julianmayr1/BoseGasCL`

[1] Kernel applied in spatial dimension only

Acronyms

BEC Bose-Einstein condensate. 26, 31, 32, 49, 56, 69

CL complex Langevin. 25, 26, 38, 48, 59, 60, 64, 65, 67, 69–71

CSPI coherent state path integral. 10, 14, 15, 19, 20, 57, 58

EP easy plane. 30, 31, 61, 63, 65

FFT fast fourier transform. 58, 60

GPU graphics processing unit. 46, 71

HMC Hamiltonian/Hybrid Monte Carlo. 19, 70

PDF probability density function. 18–24, 26, 46, 48

QCD quantum chromodynamics. 19, 22, 69

QCP quantum critical point. 40, 62

QFT quantum field theory. 10, 38, 49, 59, 69

QPT quantum phase transition. 39

Bibliography

[1] Carlo Maria Becchi. "Second quantization". en. In: *Scholarpedia* 5.6 (June 2010), p. 7902. ISSN: 1941-6016. DOI: 10.4249/scholarpedia.7902. URL: http://www.scholarpedia.org/article/Second_quantization (visited on 01/16/2024).

[2] Michael Edward Peskin and Daniel V. Schroeder. *An introduction to quantum field theory*. en. Reading, Mass: Addison-Wesley Pub. Co, 1995. ISBN: 978-0-201-50397-5.

[3] Xiao-Gang Wen. *Quantum Field Theory of Many-Body Systems*. Oxford University Press, Sept. 2007. ISBN: 978-0-19-922725-9. DOI: 10.1093/acprof:oso/9780199227259.001.0001. URL: https://academic.oup.com/book/25836 (visited on 01/16/2024).

[4] Mark Jarrel. *Coherent State Path Integral Quantization of Quantum Field Theory*. URL: https://eduardo.physics.illinois.edu/phys582/582-chapter8-edited.pdf (visited on 11/29/2023).

[5] *Campbell-Hausdorff formula - Encyclopedia of Mathematics*. URL: https://encyclopediaofmath.org/wiki/Campbell-Hausdorff_formula (visited on 01/31/2024).

[6] Luis C. dos Santos and M. A. M. de Aguiar. *A New Form of Path Integral for the Coherent States Representation and its Semiclassical Limit*. en. arXiv:quant-ph/0412080. Dec. 2004. URL: http://arxiv.org/abs/quant-ph/0412080 (visited on 05/22/2023).

[7] Leo P. Kadanoff and Gordon Baym. *Quantum Statistical Mechanics: Green's Function Methods in Equilibrium and Nonequilibrium Problems*. en. 1st ed. CRC Press, Mar. 2018. ISBN: 978-0-429-49321-8. DOI: 10.1201/9780429493218. URL: https://www.taylorfrancis.com/books/9780429961762 (visited on 02/02/2024).

[8] Daniel Alvestad, Rasmus Larsen, and Alexander Rothkopf. "Stable solvers for real-time Complex Langevin". en. In: *Journal of High Energy Physics* 2021.8 (Aug. 2021). arXiv:2105.02735 [hep-lat], p. 138. ISSN: 1029-8479. DOI: 10.1007/JHEP08(2021)138. URL: http://arxiv.org/abs/2105.02735 (visited on 03/09/2023).

[9] Kirill Boguslavski, Paul Hotzy, and David I. Müller. "Stabilizing complex Langevin for real-time gauge theories with an anisotropic kernel". en. In: *Journal of High Energy Physics* 2023.6 (June 2023). arXiv:2212.08602 [hep-lat, physics:hep-ph], p. 11. ISSN: 1029-8479. DOI: 10.1007/JHEP06(2023)011. URL: http://arxiv.org/abs/2212.08602 (visited on 10/03/2023).

[10] Jürgen Berges et al. “Lattice simulations of real-time quantum fields”. In: *Physical Review D* 75.4 (Jan. 2007). MAG ID: 2071844098, p. 045007. DOI: 10.1103/physrevd.75.045007.

[11] Kurt Binder and Dieter W. Heermann. *Monte Carlo Simulation in Statistical Physics: An Introduction*. en. Vol. 0. Graduate Texts in Physics. Berlin, Heidelberg: Springer Berlin Heidelberg, 2010. ISBN: 978-3-642-03162-5 978-3-642-03163-2. DOI: 10.1007/978-3-642-03163-2. URL: https://link.springer.com/10.1007/978-3-642-03163-2 (visited on 04/25/2023).

[12] Mark E. J. Newman and Gerard T. Barkema. *Monte Carlo methods in statistical physics*. en. Reprinted (with corr.) Oxford: Clarendon Press [u.a.], 2010. ISBN: 978-0-19-851796-2 978-0-19-851797-9.

[13] Nicholas Metropolis et al. “Equation of State Calculations by Fast Computing Machines”. en. In: *The Journal of Chemical Physics* 21.6 (June 1953), pp. 1087–1092. ISSN: 0021-9606, 1089-7690. DOI: 10.1063/1.1699114. URL: https://pubs.aip.org/jcp/article/21/6/1087/202680/Equation-of-State-Calculations-by-Fast-Computing (visited on 01/16/2024).

[14] M. J. Betancourt et al. *The Geometric Foundations of Hamiltonian Monte Carlo*. en. arXiv:1410.5110 [stat]. Oct. 2014. URL: http://arxiv.org/abs/1410.5110 (visited on 01/16/2024).

[15] W. M. C. Foulkes et al. “Quantum Monte Carlo simulations of solids”. en. In: *Reviews of Modern Physics* 73.1 (Jan. 2001), pp. 33–83. ISSN: 0034-6861, 1539-0756. DOI: 10.1103/RevModPhys.73.33. URL: https://link.aps.org/doi/10.1103/RevModPhys.73.33 (visited on 01/24/2024).

[16] M Tanabashi. “17.1 Lattice regularization of QCD”. en. In: (2019).

[17] Ulli Wolff. “Triviality of four dimensional phiˆ4 theory on the lattice”. en. In: *Scholarpedia* 9.10 (Oct. 2014), p. 7367. ISSN: 1941-6016. DOI: 10.4249/scholarpedia.7367. URL: http://www.scholarpedia.org/article/Triviality_of_four_dimensional_phi%5E4_theory_on_the_lattice (visited on 01/16/2024).

[18] Hans De Raedt and Ad Lagendijk. “Monte Carlo simulation of quantum statistical lattice models”. en. In: *Physics Reports* 127.4 (Oct. 1985), pp. 233–307. ISSN: 03701573. DOI: 10.1016/0370-1573(85)90044-4. URL: https://linkinghub.elsevier.com/retrieve/pii/0370157385900444 (visited on 02/02/2024).

[19] Christof Gattringer and Kurt Langfeld. “Approaches to the sign problem in lattice field theory”. en. In: *International Journal of Modern Physics A* 31.22 (Aug. 2016). arXiv:1603.09517 [hep-lat], p. 1643007. ISSN: 0217-751X, 1793-656X. DOI: 10.1142/S0217751X16430077. URL: http://arxiv.org/abs/1603.09517 (visited on 03/07/2023).

[20] V I Tatarskiĭ. “The Wigner representation of quantum mechanics”. en. In: *Soviet Physics Uspekhi* 26.4 (Apr. 1983), pp. 311–327. ISSN: 0038-5670. DOI: 10.1070/PU1983v026n04ABEH004345. URL: https://iopscience.iop.org/article/10.1070/PU1983v026n04ABEH004345 (visited on 01/24/2024).

[21] Casey E. Berger et al. “Complex Langevin and other approaches to the sign problem in quantum many-body physics”. en. In: *Physics Reports* 892 (Jan. 2021). arXiv:1907.10183 [cond-mat, physics:hep-lat, physics:nucl-th], pp. 1–54. ISSN: 03701573. DOI: 10.1016/j.physrep.2020.09.002. URL: http://arxiv.org/abs/1907.10183 (visited on 03/07/2023).

[22] Robert Zwanzig. *Nonequilibrium statistical mechanics*. en. Oxford ; New York: Oxford University Press, 2001. ISBN: 978-0-19-514018-7.

[23] Glenn H. Fredrickson and Kris T. Delaney. *Field-Theoretic Simulations in Soft Matter and Quantum Fluids*. en. 1st ed. Oxford University PressOxford, Feb. 2023. ISBN: 978-0-19-284748-5 978-0-19-193977-8. DOI: 10.1093/oso/9780192847485.001.0001. URL: https://academic.oup.com/book/45705 (visited on 06/14/2023).

[24] Grigorios A. Pavliotis. *Stochastic Processes and Applications: Diffusion Processes, the Fokker-Planck and Langevin Equations*. en. Vol. 60. Texts in Applied Mathematics. New York, NY: Springer New York, 2014. ISBN: 978-1-4939-1322-0 978-1-4939-1323-7. DOI: 10.1007/978-1-4939-1323-7. URL: https://link.springer.com/10.1007/978-1-4939-1323-7 (visited on 01/16/2024).

[25] Giorgio Parisi. “On complex probabilities”. en. In: *Physics Letters B* 131.4-6 (Nov. 1983), pp. 393–395. ISSN: 03702693. DOI: 10.1016/0370-2693(83)90525-7. URL: https://linkinghub.elsevier.com/retrieve/pii/0370269383905257 (visited on 10/17/2023).

[26] Giorgio Parisi and Yong-Shi Wu. “PERTURBATION-THEORY WITHOUT GAUGE FIXING”. In: *Science of Sintering* 24.4 (Apr. 1981). MAG ID: 1573631469 S2ID: f3ffcfefd65573eb57445f94158066afa0b1dd83, pp. 483–496. DOI: 10.1360/ya1981-24-4-483.

[27] Gert Aarts, Erhard Seiler, and Ion-Olimpiu Stamatescu. “The Complex Langevin method: When can it be trusted?” en. In: *Physical Review D* 81.5 (Mar. 2010). arXiv:0912.3360 [cond-mat, physics:hep-lat, physics:hep-th, physics:math-ph], p. 054508. ISSN: 1550-7998, 1550-2368. DOI: 10.1103/PhysRevD.81.054508. URL: http://arxiv.org/abs/0912.3360 (visited on 10/18/2023).

[28] Erhard Seiler. “Status of Complex Langevin”. en. In: *EPJ Web of Conferences* 175 (2018). arXiv:1708.08254 [hep-lat], p. 01019. ISSN: 2100-014X. DOI: 10.1051/epjconf/201817501019. URL: http://arxiv.org/abs/1708.08254 (visited on 10/18/2023).

[29] John R. Klauder and Wesley P. Petersen. “Spectrum of certain non-self-adjoint operators and solutions of Langevin equations with complex drift”. en. In: *Journal of Statistical Physics* 39.1-2 (Apr. 1985), pp. 53–72. ISSN: 0022-4715, 1572-9613. DOI: 10.1007/BF01007974. URL: http://link.springer.com/10.1007/BF01007974 (visited on 01/16/2024).

[30] Gert Aarts et al. “Adaptive stepsize and instabilities in complex Langevin dynamics”. en. In: *Physics Letters B* 687.2-3 (Apr. 2010). arXiv:0912.0617 [hep-lat, physics:hep-th, physics:nucl-th], pp. 154–159. ISSN: 03702693. DOI: 10.1016/j.physletb.2010.03.012. URL: http://arxiv.org/abs/0912.0617 (visited on 01/16/2024).

[31] Keitaro Nagata, Jun Nishimura, and Shinji Shimasaki. “Justification of the complex Langevin method with the gauge cooling procedure”. en. In: *Progress of Theoretical and Experimental Physics* 2016.1 (Jan. 2016). arXiv:1508.02377 [cond-mat, physics:hep-lat, physics:hep-th], 013B01. ISSN: 2050-3911. DOI: 10.1093/ptep/ptv173. URL: http://arxiv.org/abs/1508.02377 (visited on 10/17/2023).

[32] Matthias Troyer and Uwe-Jens Wiese. “Computational complexity and fundamental limitations to fermionic quantum Monte Carlo simulations”. In: *Physical Review Letters* 94.17 (May 2005). MAG ID: 2017474131, p. 170201. DOI: 10.1103/physrevlett.94.170201.

[33] Lena Funcke et al. “Review on Quantum Computing for Lattice Field Theory”. en. In: *Proceedings of The 39th International Symposium on Lattice Field Theory — PoS(LATTICE2022)*. arXiv:2302.00467 [hep-lat, physics:quant-ph]. Feb. 2023, p. 228. DOI: 10.22323/1.430.0228. URL: http://arxiv.org/abs/2302.00467 (visited on 02/02/2024).

[34] Tin-Lun Ho. “Spinor Bose Condensates in Optical Traps”. en. In: *Physical Review Letters* 81.4 (July 1998). arXiv:cond-mat/9803231, pp. 742–745. ISSN: 0031-9007, 1079-7114. DOI: 10.1103/PhysRevLett.81.742. URL: http://arxiv.org/abs/cond-mat/9803231 (visited on 10/19/2023).

[35] Yuki Kawaguchi and Masahito Ueda. “Spinor Bose-Einstein condensates”. en. In: *Physics Reports* 520.5 (Nov. 2012). arXiv:1001.2072 [cond-mat], pp. 253–381. ISSN: 03701573. DOI: 10.1016/j.physrep.2012.07.005. URL: http://arxiv.org/abs/1001.2072 (visited on 03/27/2023).

[36] D. L. Campbell et al. “Magnetic phases of spin-1 spin–orbit-coupled Bose gases”. en. In: *Nature Communications* 7.1 (Mar. 2016), p. 10897. ISSN: 2041-1723. DOI: 10.1038/ncomms10897. URL: https://www.nature.com/articles/ncomms10897 (visited on 01/17/2024).

[37] Philipp Heinen and Thomas Gasenzer. "Complex Langevin approach to interacting Bose gases". en. In: *Physical Review A* 106.6 (Dec. 2022). arXiv:2204.10661 [cond-mat, physics:hep-lat, physics:physics], p. 063308. ISSN: 2469-9926, 2469-9934. DOI: 10.1103/PhysRevA.106.063308. URL: http://arxiv.org/abs/2204.10661 (visited on 03/07/2023).

[38] Taha Yogurt, A. Keles, and M. Oktel. *Spinor Boson Droplets Stabilized By Spin Fluctuations*. Jan. 2022.

[39] Lewis A. Williamson and P. B. Blakie. "Universal coarsening dynamics of a quenched ferromagnetic spin-1 condensate". en. In: *Physical Review Letters* 116.2 (Jan. 2016). arXiv:1504.06404 [cond-mat], p. 025301. ISSN: 0031-9007, 1079-7114. DOI: 10.1103/PhysRevLett.116.025301. URL: http://arxiv.org/abs/1504.06404 (visited on 01/18/2024).

[40] Nguyen Thanh Phuc, Yuki Kawaguchi, and Masahito Ueda. "Effects of thermal and quantum fluctuations on the phase diagram of a spin-1 87 Rb Bose-Einstein condensate". en. In: *Physical Review A* 84.4 (Oct. 2011), p. 043645. ISSN: 1050-2947, 1094-1622. DOI: 10.1103/PhysRevA.84.043645. URL: https://link.aps.org/doi/10.1103/PhysRevA.84.043645 (visited on 08/07/2023).

[41] Shun Uchino, Michikazu Kobayashi, and Masahito Ueda. "Bogoliubov Theory and Lee-Huang-Yang Corrections in Spin-1 and Spin-2 Bose-Einstein Condensates in the Presence of the Quadratic Zeeman Effect". en. In: *Physical Review A* 81.6 (June 2010). arXiv:0912.0355 [cond-mat, physics:nucl-th], p. 063632. ISSN: 1050-2947, 1094-1622. DOI: 10.1103/PhysRevA.81.063632. URL: http://arxiv.org/abs/0912.0355 (visited on 03/27/2023).

[42] Philipp Heinen. "Simulation of ultracold Bose gases with the complex Langevin method (unpublished)". PhD thesis. Feb. 2024.

[43] Charles Kittel. *Introduction to solid state physics*. en. 8th ed. Hoboken, NJ: Wiley, 2005. ISBN: 978-0-471-41526-8.

[44] Subir Sachdev. *Quantum Phase Transitions*. 2nd ed. Cambridge University Press, 2011.

[45] S. L. Sondhi et al. "Continuous Quantum Phase Transitions". en. In: *Reviews of Modern Physics* 69.1 (Jan. 1997). arXiv:cond-mat/9609279, pp. 315–333. ISSN: 0034-6861, 1539-0756. DOI: 10.1103/RevModPhys.69.315. URL: http://arxiv.org/abs/cond-mat/9609279 (visited on 04/17/2023).

[46] Peter Arnold and Guy D. Moore. *Monte Carlo simulation of O(2) phi^4 field theory in three dimensions*. en. arXiv:cond-mat/0103227. July 2003. DOI: 10.1103/PhysRevE68.049902. URL: http://arxiv.org/abs/cond-mat/0103227 (visited on 04/25/2023).

[47] K. Binder. "Critical Properties from Monte Carlo Coarse Graining and Renormalization". en. In: *Physical Review Letters* 47.9 (Aug. 1981), pp. 693–696. ISSN: 0031-9007. DOI: 10.1103/PhysRevLett.47.693. URL: https://link.aps.org/doi/10.1103/PhysRevLett.47.693 (visited on 05/04/2023).

[48] Massimo Campostrini, Andrea Pelissetto, and Ettore Vicari. "Finite-size scaling at quantum transitions". In: *Physical Review B* 89.9 (Mar. 2014). Publisher: American Physical Society, p. 094516. DOI: 10.1103/PhysRevB.89.094516. URL: https://link.aps.org/doi/10.1103/PhysRevB.89.094516 (visited on 04/16/2023).

[49] Özer Özdal. "THE HIGGS BOSON AND RIGHT-HANDED NEUTRINOS IN SUPERSYMMETRIC MODELS". en. In: (2016). Publisher: Unpublished. DOI: 10.13140/RG.2.2.18314.52165. URL: http://rgdoi.net/10.13140/RG.2.2.18314.52165 (visited on 02/02/2024).

[50] A. S. Kronfeld. "Dynamics of Langevin Simulation". en. In: *Progress of Theoretical Physics Supplement* 111 (1993). arXiv:hep-lat/9205008, pp. 293–311. ISSN: 0375-9687. DOI: 10.1143/PTPS.111.293. URL: http://arxiv.org/abs/hep-lat/9205008 (visited on 05/20/2023).

[51] G. G. Batrouni et al. "Langevin simulations of lattice field theories". en. In: *Physical Review D* 32.10 (Nov. 1985), pp. 2736–2747. ISSN: 0556-2821. DOI: 10.1103/PhysRevD.32.2736. URL: https://link.aps.org/doi/10.1103/PhysRevD.32.2736 (visited on 05/15/2023).

[52] Alan M. Ferrenberg and Robert H. Swendsen. "Optimized Monte Carlo data analysis". en. In: *Physical Review Letters* 63.12 (Sept. 1989), pp. 1195–1198. ISSN: 0031-9007. DOI: 10.1103/PhysRevLett.63.1195. URL: https://link.aps.org/doi/10.1103/PhysRevLett.63.1195 (visited on 09/11/2023).

[53] Kari Rummukainen. *MC lecture notes*. URL: https://www.mv.helsinki.fi/home/rummukai/lectures/montecarlo_oulu/lectures/mc_notes4.pdf (visited on 10/02/2023).

[54] Jacques Bloch. "Reweighting complex Langevin trajectories". en. In: *Physical Review D* 95.5 (Mar. 2017). arXiv:1701.00986 [cond-mat, physics:hep-lat], p. 054509. ISSN: 2470-0010, 2470-0029. DOI: 10.1103/PhysRevD.95.054509. URL: http://arxiv.org/abs/1701.00986 (visited on 11/27/2023).

[55] Xin-Yu Luo et al. "Deterministic entanglement generation from driving through quantum phase transitions". en. In: *Science* 355.6325 (Feb. 2017). arXiv:1702.03120 [cond-mat], pp. 620–623. ISSN: 0036-8075, 1095-9203. DOI: 10.1126/science.aag1106. URL: http://arxiv.org/abs/1702.03120 (visited on 01/26/2024).

[56] Nicolai Friis and Ivette Fuentes. "Entanglement generation in relativistic quantum fields". en. In: *Journal of Modern Optics* 60.1 (Jan. 2013). arXiv:1204.0617 [gr-qc, physics:quant-ph], pp. 22–27. ISSN: 0950-0340, 1362-3044. DOI: 10.1080/09500340.2012.712725. URL: http://arxiv.org/abs/1204.0617 (visited on 01/18/2024).

[57] U. V. Poulsen, T. Meyer, and M. Lewenstein. "Entanglement in the Bogoliubov vacuum". en. In: *Physical Review A* 71.6 (June 2005). arXiv:cond-mat/0405550, p. 063605. ISSN: 1050-2947, 1094-1622. DOI: 10.1103/PhysRevA.71.063605. URL: http://arxiv.org/abs/cond-mat/0405550 (visited on 01/18/2024).

[58] Pasquale Calabrese and John Cardy. "Entanglement Entropy and Quantum Field Theory". en. In: *Journal of Statistical Mechanics: Theory and Experiment* 2004.06 (June 2004). arXiv:hep-th/0405152, P06002. ISSN: 1742-5468. DOI: 10.1088/1742-5468/2004/06/P06002. URL: http://arxiv.org/abs/hep-th/0405152 (visited on 12/05/2023).

[59] Pasquale Calabrese, John Cardy, and Erik Tonni. "Entanglement Negativity in Quantum Field Theory". en. In: *Physical Review Letters* 109.13 (Sept. 2012), p. 130502. ISSN: 0031-9007, 1079-7114. DOI: 10.1103/PhysRevLett.109.130502. URL: https://link.aps.org/doi/10.1103/PhysRevLett.109.130502 (visited on 12/09/2023).

[60] Kai-Hsin Wu et al. "Entanglement Renyi Negativity across a Finite Temperature Transition: A Monte Carlo study". en. In: *Physical Review Letters* 125.14 (Sept. 2020), p. 140603. ISSN: 0031-9007, 1079-7114. DOI: 10.1103/PhysRevLett.125.140603. URL: https://link.aps.org/doi/10.1103/PhysRevLett.125.140603 (visited on 12/09/2023).

[61] Y. Nakagawa et al. *Entanglement entropy of SU(3) Yang-Mills theory*. en. arXiv:0911.2596 [cond-mat, physics:hep-lat, physics:hep-ph, physics:hep-th, physics:quant-ph]. Nov. 2009. URL: http://arxiv.org/abs/0911.2596 (visited on 12/05/2023).

[62] Michael A. Nielsen and Isaac L. Chuang. *Quantum Computation and Quantum Information: 10th Anniversary Edition*. 1st ed. Cambridge University Press, June 2012. ISBN: 978-1-107-00217-3 978-0-511-97666-7. DOI: 10.1017/CBO9780511976667. URL: https://www.cambridge.org/core/product/identifier/9780511976667/type/book (visited on 01/18/2024).

[63] Chia-Min Chung et al. "Entanglement negativity via replica trick: a Quantum Monte Carlo approach". en. In: *Physical Review B* 90.6 (Aug. 2014). arXiv:1312.1168 [cond-mat], p. 064401. ISSN: 1098-0121, 1550-235X. DOI: 10.1103/PhysRevB.90.064401. URL: http://arxiv.org/abs/1312.1168 (visited on 12/17/2023).

[64] Philipp Heinen and Thomas Gasenzer. *Simulating the Berezinskii-Kosterlitz-Thouless Transition with Complex Langevin*. en. arXiv:2304.05699 [cond-mat, physics:hep-lat]. Apr. 2023. URL: http://arxiv.org/abs/2304.05699 (visited on 07/17/2023).

[65] Kris T. Delaney, Henri Orland, and Glenn H. Fredrickson. “Numerical Simulation of Finite-Temperature Field Theory for Interacting Bosons”. en. In: *Physical Review Letters* 124.7 (Feb. 2020), p. 070601. ISSN: 0031-9007, 1079-7114. DOI: 10.1103/PhysRevLett.124.070601. URL: https://link.aps.org/doi/10.1103/PhysRevLett.124.070601 (visited on 05/18/2023).

[66] Yuki Kawaguchi, Nguyen Thanh Phuc, and P. Blair Blakie. “Finite-temperature phase diagram of a spin-1 Bose gas”. en. In: *Physical Review A* 85.5 (May 2012), p. 053611. ISSN: 1050-2947, 1094-1622. DOI: 10.1103/PhysRevA.85.053611. URL: https://link.aps.org/doi/10.1103/PhysRevA.85.053611 (visited on 08/06/2023).

[67] Leonardus, Laurence E. Sigler, and Leonardus. *Fibonacci's Liber abaci: a translation into modern English of Leonardo Pisano's book of calculation*. en. 1. softcover printing. Sources and studies in the history of mathematics and physical sciences. New York Berlin Heidelberg: Springer, 2003. ISBN: 978-0-387-40737-1.

[68] S. Ryu and Y. Hatsugai. “Entanglement entropy and the Berry phase in solid states”. en. In: *Physical Review B* 73.24 (June 2006). arXiv:cond-mat/0601237, p. 245115. ISSN: 1098-0121, 1550-235X. DOI: 10.1103/PhysRevB.73.245115. URL: http://arxiv.org/abs/cond-mat/0601237 (visited on 01/25/2024).

[69] J. Appel et al. “Mesoscopic atomic entanglement for precision measurements beyond the standard quantum limit”. en. In: *Proceedings of the National Academy of Sciences* 106.27 (July 2009), pp. 10960–10965. ISSN: 0027-8424, 1091-6490. DOI: 10.1073/pnas.0901550106. URL: https://pnas.org/doi/full/10.1073/pnas.0901550106 (visited on 02/05/2024).

[70] Samy Mailoud Sekkouri, Felix Izrailev, and Fausto Borgonovi. “Spectrum statistics in the integrable Lieb-Liniger model”. en. In: *Physical Review E* 104.3 (Sept. 2021). arXiv:2105.02967 [cond-mat, physics:nlin, physics:quant-ph], p. 034212. ISSN: 2470-0045, 2470-0053. DOI: 10.1103/PhysRevE.104.034212. URL: http://arxiv.org/abs/2105.02967 (visited on 02/05/2024).

[71] Bethan Cropp, Stefano Liberati, and Rodrigo Turcati. “Analogue black holes in relativistic BECs: Mimicking Killing and universal horizons”. en. In: *Physical Review D* 94.6 (Sept. 2016), p. 063003. ISSN: 2470-0010, 2470-0029. DOI: 10.1103/PhysRevD.94.063003. URL: https://link.aps.org/doi/10.1103/PhysRevD.94.063003 (visited on 02/05/2024).

[72] Tobias Dornheim et al. “Path integral Monte Carlo approach to the structural properties and collective excitations of liquid $$ˆ3{\text {He}}$$ without fixed nodes”. en. In: *Scientific Reports* 12.1 (Jan. 2022), p. 708. ISSN: 2045-2322. DOI: 10.1038/s41598-021-04355-9. URL: https://www.nature.com/articles/s41598-021-04355-9 (visited on 02/05/2024).

[73] Daniel Alvestad, Rasmus Larsen, and Alexander Rothkopf. *Kernel controlled real-time Complex Langevin simulation*. en. arXiv:2212.07985 [hep-lat]. Dec. 2022. URL: http://arxiv.org/abs/2212.07985 (visited on 01/31/2024).

[74] Pierre Monmarché. *High-dimensional MCMC with a standard splitting scheme for the underdamped Langevin diffusion*. en. arXiv:2007.05455 [math, stat]. June 2021. URL: http://arxiv.org/abs/2007.05455 (visited on 02/05/2024).

[75] Ryosuke Okuta et al. "CuPy: A NumPy-Compatible Library for NVIDIA GPU Calculations". In: *Proceedings of Workshop on Machine Learning Systems (LearningSys) in The Thirty-first Annual Conference on Neural Information Processing Systems (NIPS)*. 2017. URL: http://learningsys.org/nips17/assets/papers/paper_16.pdf.